Applied Thermal Engineering 281 (2025) 128654

Contents lists available at ScienceDirect

Applied Thermal Engineering

journal homepage: www.elsevier.com/locate/apthermeng

Research Paper

Improving the trade-off between NOx, soot, efficiency, durability in a PPCI engine: optimal design of the injection pattern via CFD simulations

Davide Viscione, Valerio Mariani *, Gian Marco Bianchi, Stefania Falfari, Vittorio Ravaglioli, Giacomo Silvagni

DIN – Dipartimento di Ingegneria Industriale, Alma Mater Studiorum – Università di Bologna, Bologna 40136, Italy

ARTICLE INFO

Keywords:
Low temperature combustion
PPCI engine
Stratified charge engine
Fuel injection pattern
Injection timing test
Emissions prediction
CFD

ABSTRACT

Literature on CFD validation of PPCI combustion are mainly conducted with automatic mesh refinement and detailed chemical kinetics for combustion. These features constraint the user to adopt supercomputers or computing clusters to fit standard simulation time, even though their accuracy in literature results is in line or below the average of conventional combustions simulation. After validation, these works approach the optimization of PPCI mainly focusing on fuel properties and piston bowl while implementing a single fuel injection. However, this choice cuts out the complexity of reproducing premixed-diffusive combustion stages typical of multiple injection with charge-temperature stratification. Few works have simulated the latter, but analyses are oriented towards the fuel mass split rather than on the design of the injection pattern. This work presents a validated CFD method based on fixed mesh and Progress Variable Model combustion model to design the injection pattern aiming at a solid efficiency, emissions and durability trade-off in a light-duty PPCI engine at mid-high load (10 bar, 14 bar Indicated Mean Effective Pressure). Considering a reference three-events pattern, the shift of the two early events is simulated. Simulations are run o affordable modern-workstations and completed within standard time. An improved configuration has been discovered, resulting in reduced soot and (–22 %) and Pressure Rise Rate (−25 %), moderate NOx reduction (−4%) and decent efficiency increase (+3%). The new pattern is spaced as: 41 deg BTDC; 15 deg BTDC; 1.7 deg BTDC. Overall, the improving shift direction is along anticipated 1st and delayed 2nd events.

1. Introduction

1.1. Framework

Over the last few decades, the emission limits imposed by regulations on transportation have been progressively tightened [1]. The Worldwide harmonized Light vehicles Test Procedure (WLTP) together with the Real Driving Emission (RDE) added from 2017, force the thermal unit of powertrains to operate in a highly demanding condition [2]. Furthermore, the European Commission has recently been considering the possibility of regulating the emissions of carbon dioxide, as it is recognized to be one of the species that mainly contribute to global warming. To encourage the reduction of CO_2 emissions, companies have been charged of heavy sanctions (95 € per g/km) by the European Commission for each car and for each g/km over the threshold value 95 gCO_2/km. Given the limitations of some electric powertrain components (in particular, batteries), and the low readiness level of the power distribution infrastructure, the use of internal combustion engines will remain heavy for a long time to come [3]. In light of the above, the decarbonisation of such engines must come with sustainable fuels as well as the implementation of high efficiency combustion modes.

Focusing on efficient combustion modes, an attractive solution suitable for market scale is Partially Premixed Compression Ignition (PPCI) operated via high pressure direct injection (typically 500 bar–700 bar) [4] of low-reactivity fuel. In a PPCI engine, closely spaced multiple injections (usually two or three) introduce fuel inside the combustion chamber, generating a highly stratified charge that autoignites according to chemical kinetics, depending on the local distribution of fuel and temperature. In PPCI engines the Pressure Rise Rate (PRR) is often used to take into consideration the effect of mixing and injection strategy on the combustion burn rate. The PRR is considered as a parameter to determine the safety of engine operations, and its

* Corresponding author.
E-mail address: valerio.mariani4@unibo.it (V. Mariani).

https://doi.org/10.1016/j.applthermaleng.2025.128654
Received 30 July 2025; Received in revised form 18 September 2025; Accepted 6 October 2025
Available online 9 October 2025

maximum value should not exceed 10 bar/deg. Moreover, this index is correlated with the pollutants released during the combustion event [5,6]. The injection pattern is one of the key design features that control the main aspects of interest of combustion i.e., efficiency, emissions, safety and durability, repeatability. The Start Of Injection (SOI) of each injection event determines the shape of the Rate of Heat Release (RoHR), the split of fuel injection into multiple pulses is beneficial for the reduction of the peak burn as well as for the improvement of the combustion phasing [7–11].

It is well known that the design and analysis of internal combustion engines can be successfully supported by three-dimensional Computational Fluid Dynamics (CFD) simulations. However, in the framework of PPCI combustion, CFD simulations may struggle to capture the real energy release law because of the presence of both a premixed phase, and a diffusive phase along the combustion progress. To the best knowledge of the authors, few published works have shown accurate combustion simulation results. In these works, common validation metrics are: pressure and ROHR traces; the Crank Angle at which the mass fuel burnt is 10 % (CA10), 50 % (CA50), 90 % (CA90); PRR; emissions (NOx, soot, CO, HC); efficiency/fuel consumption. In [12,13] Badra et al. have performed the CFD simulation of a GCI engine at low Indicated Mean Effective Pressure (IMEP) triggered by a single injection event with different SOI settings. The results have shown an encouraging performance of the method, however, significant relative error values have been detected on some validation metrics, especially shifting the SOI towards the TDC: up to + 165 % on PRR, up to 22 % on CA50, up to 65 % on NOx, up to 60 % on soot, etc. The increasing error with the SOI upward shifting is likely due to the hard reproduction of the local mixing at the Start Of Combustion (SOC) as the injection event comes closer. In [14] Sim et al. have shown the validation of a CFD methodology used to simulate the same engine as that in [13] at low and mid loads using a single injection positioned at a highly anticipated timing. The simulated specific fuel consumption and emissions match the experimental results. The simulated pressure trace and RoHR at low load are in line with the experiments, while significant overestimation has been recorded at mid load. In [15] Kim et al. have published a simulation work focused on a GCI engine triggered by a single injection using alkylate as fuel. The simulations have been aimed at reproducing the results of a real engine operating under low load. The authors have run multi-cycle simulations to capture fuel and temperature stratification in a better manner. The indicating analysis have shown good agreement with experiments and an improvement of the accuracy going on with simulated cycles. In [16] Addepalli et al. have presented the CFD simulation of a heavy-duty GCI engine triggered by different injection patterns (two and three injection events). The validation has proven a high accuracy of the CFD simulation on the prediction of the metrics except for the RoHR and the CA90. In particular, the diffusive phase of the RoHR has been captured quite well, while the simulated premixed phase of the RoHR has shown higher and delayed peaks compared to the experiments.

1.2. Contribution

To the best knowledge of the authors, all the cited CFD works relies on the use of SAGE detailed chemistry solver and Adaptive Mesh Refinement (AMR), both known to be highly demanding in terms of computing power and memory. This setup may fit standard computational resources in simulations of engines fuelled with gaseous fuels (e.g., hydrogen and methane) due to the lack of heavy mesh refinements along the spray plumes, and the small size of the kinetics schemes of those fuels. The simulation of liquid fuels would require heavier refinements and larger schemes. Furthermore, it is reported that the validation shown in [12–15] is focused on a single injection event that leads to an almost fully premixed shape of the RoHR, that may not be representative of the typical shape yielded from multiple injections (e.g., the one validated in [16]). Therefore, the valuable accuracy of the methodology cannot be directly extended to complex injection patterns.

Most of the cited works are focused on the use of CFD to predict: the effect of the wall temperature [15]; the piston bowl shape [13,14,17]; the geometric characteristics of the injector (number of nozzles, diameter of nozzle, spray angle) [18]; and fuel properties [17]. Few numerical works provide insights and detailed analyses on the design of the injection pattern to improve the key aspects of PPCI (NOx, soot, efficiency, PRR). In [17] Moiz et al. have also presented the difference between a double-injection pattern and a triple injection pattern on the simulated emissions and pressure curves of a GCI engine at high load. In [16] Addepalli et al. used their validated CFD methodology to investigate the effect of the mass split between two injection events as well as that of moving only the main injection. However, hints on the design of the pattern in terms of SOI positioning and spacing of the earlier injection events are missing.

In this work, the authors present the CFD simulation of a PPCI combustion triggered by a three-events injection pattern using CFD simulations based on fixed mesh and combustion progress variable modelling, which can fit the computing power of standard-performance workstations. The proposed setup has been validated against experimental data from a reference PPCI engine operating on two different points (mid load IMEP = 10 bar, and mid-high load IMEP = 14 bar) characterized by both the premixed and diffusive combustion phases, whose numerical reproduction has been poorly investigated in the literature. The CFD methodology has been extensively validated comparing the pressure trace, the RoHR, the specific NOx and soot, and the maximum pressure rise rate. The presented methodology can match, or even outperform (especially focusing on PRR, NOx and RoHR), the accuracy shown in similar works based on AMR and SAGE [12,13,16].

Once the CFD methodology has been validated, it has been used to give a view on the effect of moving the Start Of Injection (SOI) of the Pre and the Pilot events as well as the dwell time between these two. Eight different injection patterns have been designed to identify the way these two key preliminary injection events affect the response of the engine. The focus has been posed on emissions (CO, soot, NOx), indicated performance (efficiency, combustion angles), pressure rise rate and mixing quality. Eventually, the response of the engine to the shift of Pre and Pilot has been mapped, and the maps reveal an injection pattern that leads to a new solid trade-off between emissions, efficiency and durability of the engine mainly characterized by a strong reduction of soot emission and PRR (particularly important at mid-high load) as well as an improved efficiency. For the sake of clarity, the main points of the literature review discussed above is summarized in Table 1 together with those of the present work.

2. Methodology

2.1. Computational setup

To perform the CFD simulations, the commercial software Star-CD v 4.28 by Siemens has been used. The meshed engine is a GCI-operated Diesel head installed on a test bench and it has been experimentally characterized by some of the present authors [19]. The real engine features a flat head and a bow-shaped piston surface (CAD model in Fig. 1a, Fig. 1b). The injector, centrally installed on the flat head of each cylinder, features seven identical nozzle holes, thus, a symmetry of the physical process inside the chamber can be assumed. The symmetry has been proved in [20] by performing the CFD simulation of the full engine geometry. Therefore, to save computation time, in this work the computational domain is a 1/7 sector (Fig. 1c) of the complete combustion chamber (Fig. 1a, Fig. 1b). The main characteristics of the computation mesh are shown in Table 2. Since PPCI engines lack of spark plug and flame kernel, mesh refinements up to small cell size (0.25 mm–0.5 mm) to capture those features are not mandatory. Furthermore, it underlined that the Lagrangian approach commonly used to trace spray droplets assumes “dispersed parcels”, i.e. the continuum (namely, the cells) must be sufficiently larger than the diameter

Table 1
Literature review of papers on the CFD validation and analysis of PPCI engine. All the works in the table have been conducted by using AMR for meshing, and SAGE for combustion.

Reference	Test IMEP	Computational domain	Injection pattern	Studied effect	Validation metrics
[12,13]	6 bar	Full chamber	Single	Fuel properties	Pressure, CA50, PRR, NOx, fuel consumption
[14]	6 bar 11 bar	Full chamber	Single	Piston bowl shape	Pressure, RoHR, NOx, soot, fuel consumption
[15]	5 bar 6.5 bar	Full chamber	Single	Wall temperature	Pressure, RoHR
[16]	16.5–17.5 bar	Full chamber	Multiple (2–3)	Injection mass split	Pressure, RoHR, IMEP, CA10-50–90, efficiency
[17]	19 bar	Full chamber	Multiple (2–3)	Piston bowl shape, post injection, fuel properties	Pressure, RoHR, NOx, soot, CO, HC
This work	10–14 bar	Sector	Multiple (3)	Injection pattern (SOI shift)	Pressure, RoHR, PRR, NOx, soot

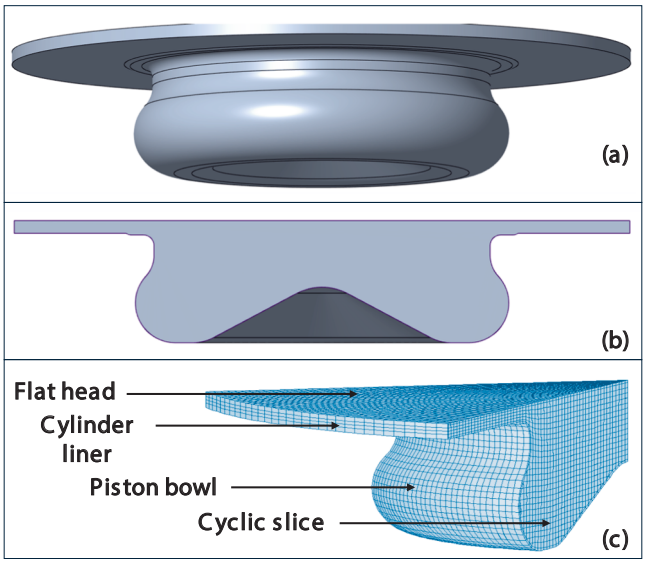

Fig. 1. Solid model of the combustion chamber (a, full geometry, (b, axial section); mesh of the computational domain (1/7 sector) (c).

Table 2
Characteristics of the computation mesh.

Feature	Value
Cell type	Hexahedra
Cell size	1 mm – uniform
Local refinement	No
Boundary layer	No
# Cells at BDC (Bottom Dead Center)	198,168
# Cells at TDC (Top Dead Center)	32,360

of the droplets.

As for the boundary conditions, the flat head, the cylinder liner and the piston bowl have been set as walls at fixed temperature (450 K). The two slice that bounds the domain in the circular direction have been set as cyclic, in order to describe the circular repetition of the face-resolved variables. The values of the initial conditions (pressure, temperature, swirl ratio, composition) inside the cylinder have been calculated thanks to the one-dimensional software GT-Power for each test point. More details about the setup in GT-Power can be found in [21].

The solution algorithm is the Pressure Implicit with Splitting Operators (PISO), and second-order central differencing schemes for momentum, turbulence, temperature, and density have been adopted. Out of the injection and of the combustion phases, the engine cycle has been discretized with a fixed angle step of 0.1 degrees (order of 8μ s). From the injection event on, the angle step has been progressively reduced to 0.05 and to 0.025 degrees (order of 1–2 μs) up to the end of the simulation.

2.2. Modelling setup

The Reynolds Averaged Navier-Stokes (RANS) approach has been used, with the $k-\epsilon$ RNG model for turbulence. The fuel spray is simulated in a Lagrangian manner including the models for atomization, breakup, and wall-impingement. The fuel spray setup, which is resumed in Table 3, has been successfully validated on previous studies of the same authors [22,23] on optical experimental data collected for gasoline injected at PPCI-like conditions in a vessel.

As a combustion model, the PVM-MF (Progress Variable Model–Multi Fuel [24]) has been used since it has led to a nice validation on low load PPCI operation points published a previous work by the same authors [21]. On Star-CD, the PVM-MF combustion model is based on the tabulated chemical kinetics (304 species, 2019 elementary reactions) of a PRF95 (Primary Reference Fuel 95 % *iso*-octane and 5 % n-heptane). The library in the PVM-MF model contains a set of solutions for an ordinary differential equation describing a static reaction system at constant pressure with enthalpy conservation. The system is in the form of Eq (1):

$$\rho \frac{dX}{dt} = \dot{\omega} \tag{1}$$

where X is the array containing the mass fraction of the chemical species and $\dot{\omega}$ is the reaction rate associated to each species. The solution of Eq. (1) is in function of pressure, enthalpy, equivalence ratio, exhaust residual ratio and a variable named Combustion Progress Variable. Such variable lies between zero and one, corresponding to the unburned and equilibrium conditions, respectively. Beyond from the mixture's mean property parameters and the species mass fractions, the library contains the Combustion Progress Variable derivative, which determines the combustion speed. Compared to conventional ECFM models, the transport of the turbulent flame surface area is not involved, thus, the results of PVM are not strictly bonded to the tuning of the alfa flame surface coefficient required by ECFM.

It is underlined that even adopting the validated spray methodology together with PVM-MF combustion model accuracy cannot be perfect. This is mainly due to some intrinsic limitations of the models, that are enhanced in stratified charge-temperature combustion (e.g., PPCI). The main limitations are the following:

- spray models rely on the introduction of "parcels" as Lagrangian units inside the continuum domain. A parcel is a unit that is statistically representative of a number of droplets that share the same

Table 3
List of models used for the CFD simulations.

Phenomenon	Model
Atomization	Huh & Gosman
Break-up	Reitz and Diwakar
Particle-wall interaction	Bai-ONERA
Leidenfrost effect	Habchi

characteristics (diameter, velocity). This use of the Lagrangian approach is necessary in order to limit the computation time, since the tracing and resolution of each droplet would be unaffordable. However, current high-pressure sprays are highly dense, thus, using parcels instead of droplets may affect the proper representation of the momentum transfer during breakup as well as the heat transfer during the wall-impingement.

- breakup models and wall-impingement models are based on empirical observations while they are made to capture aleatory phenomena. For example, the number of child droplets detached by a parent droplet during breakup, or during splash in wall-impingement is usually set at two. However, depending on the complex equilibrium of the droplet surface, two to four child droplets may be generated. Such approximations may influence the mass split between liquid phase and vapor phase.
- PVM-MF combustion model is based on pre-computed tables of the auto-ignition delay for a representative low reactivity fuel (the above mentioned PRF95). Pre-computed tables enable reduced computing time compared to detailed chemical kinetics simulation. However, in such manner, PVM-MF may struggle to predict the auto-ignition time, because PRF95 (as any other PRF) does not include aromatics, that are present in real distilled fuels.

To capture the formation of NOx and soot, the models described by Baulch et al. [25] and that by Mauss et al. [26] have been used, respectively. The CO emission has been treated with the four-step CO-CO_2 kinetics from Hautman et al. [27].

2.3. Fuel specifications

The fuel used in the present simulation setup is the Gasoline1, a pseudo-pure fluid included in the database of the CFD software Star-CD. The Gasoline1 is a Toluene Reference Fuel (TRF) given by the combination of toluene, *iso*-octane and n-heptane in a manner that the average properties are representative of those of the pump gasoline. During the simulation, the average properties of the pseudo-pure are calculated depending on the pressure and temperature values inside the cell. Table 4 shows a comparison between the main properties of Gasoline1 and those of the pump gasoline, which was the fuel used in the real GCI engine at the test bench.

Even though some relevant differences can be detected between simulation fuel and reference fuel, the general validity of the results is not compromised. Dynamic viscosity and density are mainly involved in the computation of Weber number and Ohnesorge number, which are used in determining the droplet regime in spray breakup and spray-wall impingement models. Due to the very high injection pressure used in nowadays injectors, values of Weber and Ohnesorge are usually way above the upper thresholds of those models, unavoidably leading to strip and splash, respectively. Therefore, slight shifts of viscosity and density would not affect the outcomes of spray models significantly. Furthermore, it is reported that the heat of vaporization of simulation fuel may lead to local overestimation of the gas temperature around the impingement points.

Table 4
List of the main properties of the Gasoline1 and of the pump gasoline.

Properties	Gasoline1	Pump Gasoline (EU5)
Composition (%w)	41.2 % toluene 44.4 % *iso*-octane 14.4 % n-heptane	n.d.
Molecular weight (g/mol)	101.9	100–105
Viscosity @20 °C (mPa·s)	0.49	0.39
Density @15 °C (kg/L)	0.757	0.753
Lower Heating Value (MJ/L)	32.4	30–33
Heat of vaporization (kJ/kg)	382	421

2.4. Grid sensitivity test

In order to evaluate the sensitivity of the results to the choices made on the grid, a sensitivity analysis has been conducted (Fig. 2). Specifically, the reference mesh (blue) has been coarsened by halving the number of cells along the radial direction (green), and then along the axial direction (pink). Comparing the results on different cases (Fig. 2 shows a reference case) it is visible that a coarser grid, regardless of the coarsening direction, leads to almost the same accuracy loss. Due to the best match with experimental results, the finer mesh (blue) has been adopted for the simulation campaign.

The computation time on a relatively modern workstation (parallel run on 64 GB RAM, 32 intel cores) is weakly affected by the tested number of cells, since the total CPU time ranges from 4 h (green, pink) to 6 h (blue). Even though the time difference between coarser grids and the finer grid is relatively high, simulations that take from few hours to about ten hours to complete the closed-valves engine cycle are within the standard. In face of the weak disadvantage of the computation time, using the finer mesh features a significant accuracy gain, especially on derivatives quantities (e.g. barely 5 J/deg against more than 10 J/deg on RoHR).

As the adopted software does not allow the use of AMR, a direct comparison (accuracy and computation time) between the two meshing procedures cannot be pursued.

3. Results: Validation

In this section, the results provided by the simulation have been compared with the ones measured during the experiments at the test bench. In particular, the comparison will be based on the pressure trace, the RoHR, the PRR and on the emissions of NOx and soot. For the sake of clarity, a schematic of the reference test bench is reported in Fig. 3. The cylinder highlighted in orange (the #3) is the one chosen for this study, since it was the one less affected by the cycle-to-cycle variations according to the experimental indicating analysis. The experimental results have been measured by means of the following equipment:

- pressure trace has been measured at 100 kHz with a piezoresistive pressure sensor Kistler 4067A. To reduce the signal noise, the pressure trace has been filtered with a low-pass filter set at 2.5 kHz. After collecting 100 consecutive cycles, the mean pressure trace has been obtained and used as the reference. The mean pressure trace has been postprocessed to determine the RoHR and the PRR. The RoHR has been calculated according to Eq. (2) (γ is the specific heat ratio, V is the instantaneous displacement, p is the pressure, θ is the crank angle), while the PRR has been calculated as the crank angle-derivative of the pressure trace, discretized with a first order Euler approximation.

$$RoHR(\theta) = \frac{\gamma}{\gamma - 1} V(\theta) \frac{dp(\theta)}{d\theta} + \frac{1}{\gamma - 1} p(\theta) \frac{dV(\theta)}{d\theta} \tag{2}$$

- NOx emissions have been measured with a Continental SNS14 NOx sensor that records the Parts Per Million (PPM) at the exhaust tailpipe. The ppm data have been recorded from the experiments and have been converted into g/kWh according to the procedure described in regulation [28].
- soot emissions have been measured with an AVL Smoke Meter 415S used to count the Filtered Smoke Number (FSN) during the experiments, which is based on the smoke opacity.

Firstly, the CFD methodology has been validated against two different pairs of speed and load (both medium–high load), each one actuated with four different combustion phasing (angle at 50 % of mass

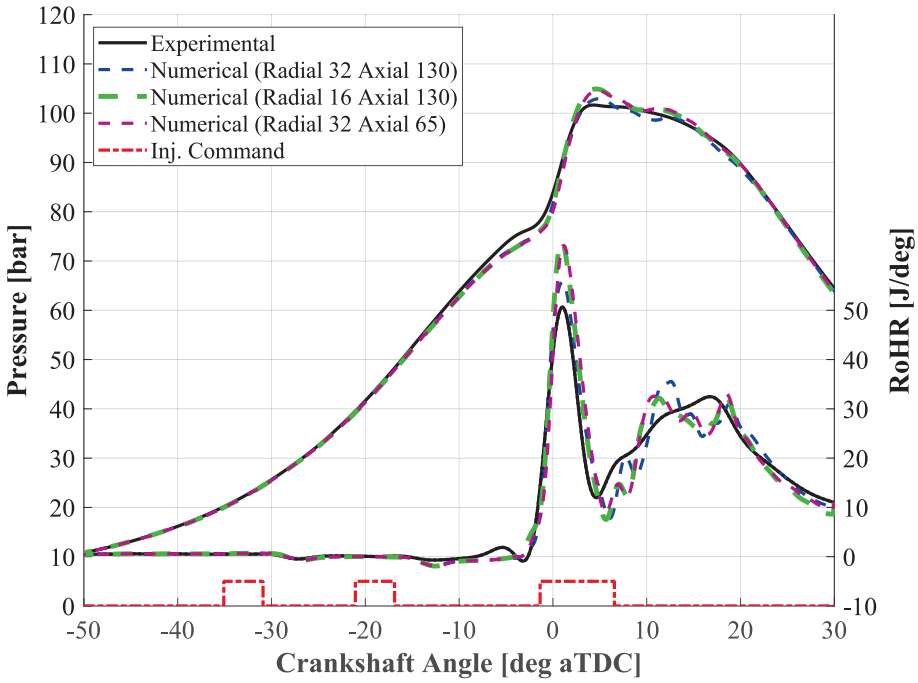

Fig. 2. Results of the grid sensitivity test on a reference operating point.

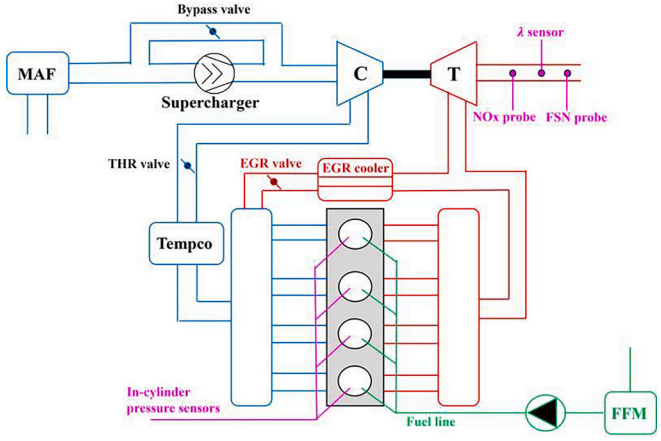

Fig. 3. Schematic of the experimental layout including the air line (blue), the fuel line (green), the exhaust gas line (red), the sensors (pink), the 4-cylinders engine block (gray), and the cylinder under investigation (orange).

burnt, CA50). In these conditions, the injection pattern is considerably different, enhancing the general validity of the proposed methodology. Table 5 lists the validation points, together with the associated injection pattern. At given speed and load, the SOI and the Energizing Time (ET) of the pilot and of the pre injection events are fixed. The values of SOI and ET have been applied to the injection controller in order to achieve the target values of Indicated Mean Effective Pressure (IMEP) and CA50. For each point, the values of the coefficient of variation $\left(COV_x = \frac{std(x)}{mean(x)}\right)$ of IMEP and of CA50 calculated on experimental data are reported in the figures.

Fig. 4 shows the experimental and simulated pressure trace and RoHR at 2000 rpm with four different SOI timings for the main injection (Point A1 to Point A4 in Table 5). The electric signal that represents the injection pattern is reported in red at the bottom of the figure. In general, the first two injections provide the early heat release in a premixed manner, owing to pressure and temperature increasing. This approach is beneficial to reduce the ignition delay of the fuel introduced during the main pulse, enhancing the combustion phasing controllability. Overall, a nice agreement between the shape of the numerical profiles and those of the experimental ones is visible. Focusing on Point A1, the numerical RoHR in the premixed phase shows a higher peak that leads to a higher energy released before the main SOI, thus, to a slightly higher pressure. The numerical diffusive RoHR, despite its pulsating oscillations, is in line with the experimental trend. Moving from Point A1 to Point A4, the dwell-time between Pre injection and Main injection is reduced, and the transition from premixed to diffusive heat release is smoother for both experimental and numerical profiles. Moreover, as the dwell-time is

Table 5
Description of the experimental points for the validation procedure.

Quantity	Point A1	Point A2	Point A3	Point A4	Point B1	Point B2	Point B3	Point B4
Engine speed [rpm]	2000				2250			
IMEP [bar]	10				14			
Intake temperature [°C]	45				50			
Intake pressure [bar]	1.8				1.9			
SOI Pilot, Pre [deg bTDC]	35, 21				41, 25			
ET Pilot, Pre [μs]	350, 350				350, 350			
SOI Main [deg bTDC]	−0.2	1.2	1.7	3.7	2.7	4.2	5.7	8.3
ET Main [μs]	556	501	471	447	647	623	590	602
CA50 [deg aTDC]	8	10	12	14	8	10	12	14

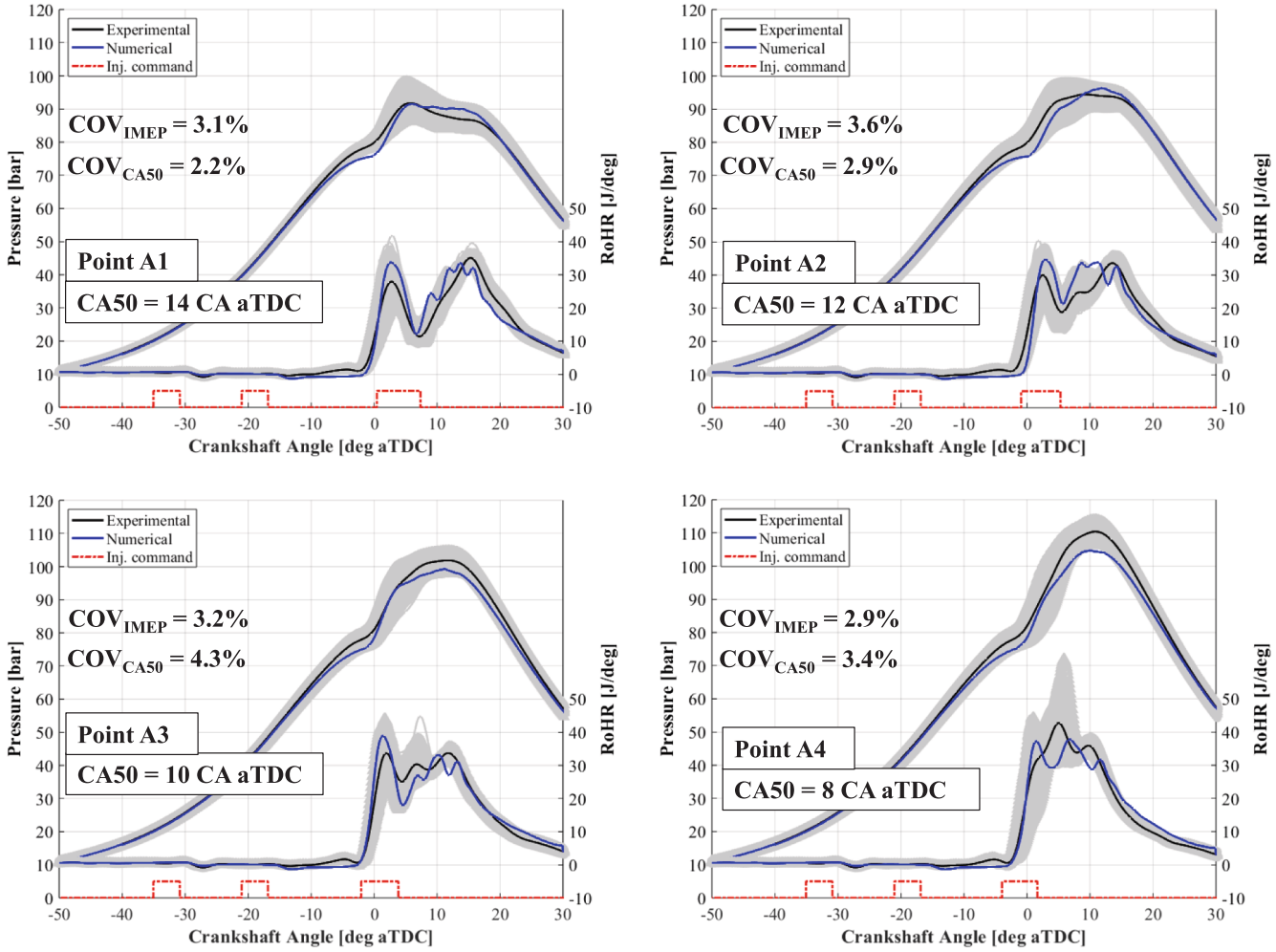

Fig. 4. Comparison between the experimental and simulated pressure and RoHR traces for Points A1 to Point A4.

reduced the accuracy of the simulation improves. For Point A4, the duration of the premixed phase in the numerical profile is longer likely due to the interaction between the progress variable and the fuel spray. In fact, the fuel spray is a source term in the transport equation for the combustion progress variable derivative.

All the numerical results lie in the grey area, which is bounded by the faster and the slower experimental cycles. Points A1 to A4 show values of the COV (both IMEP and CA50) close to the limit value usually considered for repeatable operations (3 %). It is underlined that: i) the experimental mean cycle is an approximation that may not precisely occur in the real engine (being the results of the averaging over 100 real cycles); ii) LTCs are more prone to cycle-cycle variability. Therefore, the consistency between numerical and experimental results should be evaluated on the median position of the numerical profiles inside the cycle-cycle variability area and on the overall shape, and not on the precise overlap on the mean cycle.

Fig. 5 compares the maximum PRR during the cycle for both the experimental and numerical pressure traces. The experimental red error bars show the span of the maximum PRR obtained over the 100 cycles. Instead, the values corresponding to the experimental bars correspond to the mean value of the PRR. The difference between the numerical maximum PRR and the experimental mean maximum PRR is below 1 bar/deg for any test point. Considering that and all the values are well below the 10 bar/deg safety threshold, we can say that the numerical PRR is representative of that inside the real engine. Moreover, the maximum numerical PRR lie in the experimental error bars.

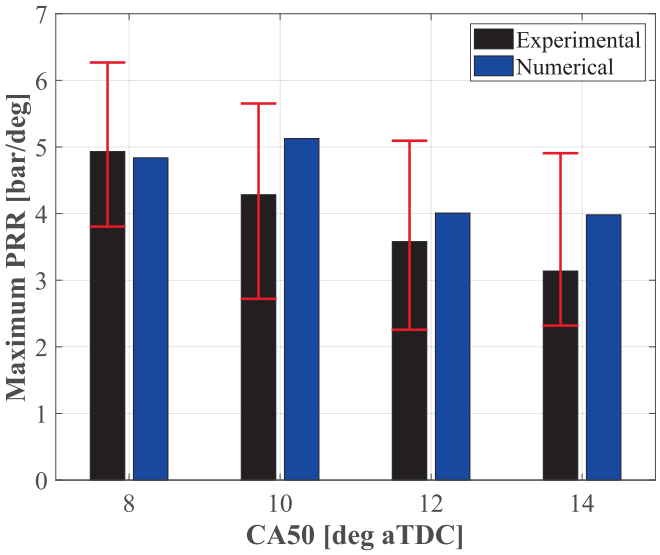

Fig. 5. Comparison between the experimental and simulated maximum PRR for Point A1 to A4.

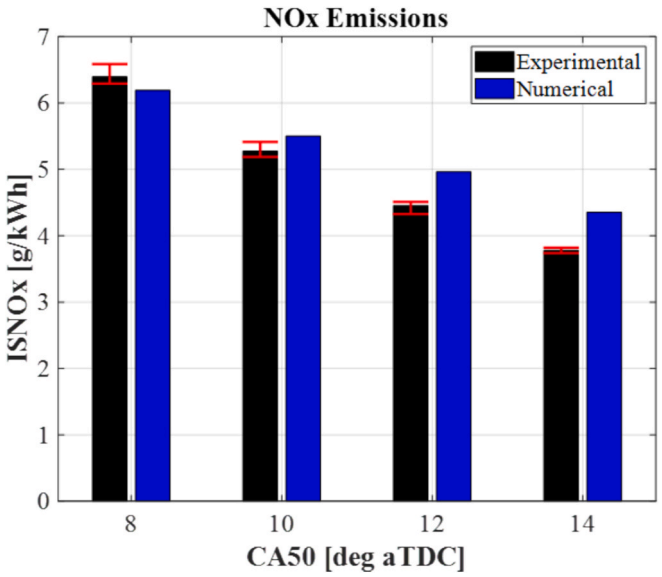

Fig. 6. Comparison between experimental and simulated ISNOx emissions for Points A1 to A4.

Moving on the NOx emissions, Fig. 6 shows both experimental and simulated values of the Indicated Specific NOx (ISNOX) for Points from A1 to A4. It is visible that the simulation is able to capture the dependence of the ISNOx on the CA50, and the punctual values as well are consistent with the experimental measure. It is highlighted that even though the simulated ISNOx is out of the experimental error bars at any CA50, the maximum error would be around 6 %.

Focusing on the soot emissions, since the FSN measurement is directly related to the opacity of the smoke, specific values for the experimental soot mass couldn't be addressed [29]. In order to make a fair comparison between the experimental measurement (in FSN) and the numerical soot mass (in kg/cycle), it is necessary to prove the strength of the correlation between these two. To this aim, the Pearson coefficient ρ between the experimental and the numerical values has been calculated according to Eq. (3), where cov(A, B) is the covariance of A and B, and σ_A and σ_B are the standard deviations of A and B. In this case, A and B are the experimental and numerical quantities, respectively.

$$\rho = \frac{cov(A,B)}{\sigma_A \sigma_B} \tag{3}$$

Fig. 7 shows the correlation between the experimental FSN and the soot mass from the CFD simulations, the value of the Pearson coefficient is 0.984. Both the high value of the Pearson coefficient and the linear shape of the curve prove that for a comparative analysis, the CFD simulation would be able to capture the differences between different injection solutions in terms of soot emissions.

In Fig. 8 it is visible the comparison between experiments and simulations in points from B1 to B4, in which the injection phasing changes, while the hydraulic delay between the electrical EOI and effective SOI has been taken as constant (350 μs). As seen for Points A1-A4, the overall shape of the simulated results matches the experimental traces. The experimental points at higher load and speed (Fig. 8) are characterized by a lower cycle dispersion, indeed the grey bounding areas are smaller compared to those at lower load and speed shown in Fig. 4. In spite of the tighter distance between the faster cycle and the slower cycle, the numerical traces are reasonably comprised in the experimental cycle-cycle variation as seen in Fig. 4. At higher load and speed, the reproduction of the shape of both the premixed and the diffusive heat release is improved as well as that of the pressure trace. Since the COV of IMEP and CA50 for points B1 to B4 is significantly lower than that seen for points A1 to A4, the representativeness of the numerical results in these cases is enhanced.

Fig. 9 shows the comparison between the maximum PRR for points from B1 to B4. Compared to the previous cases, the PRR of some of the numerical cycles (CA50 10 and 12 deg aTDC) is overestimated compared

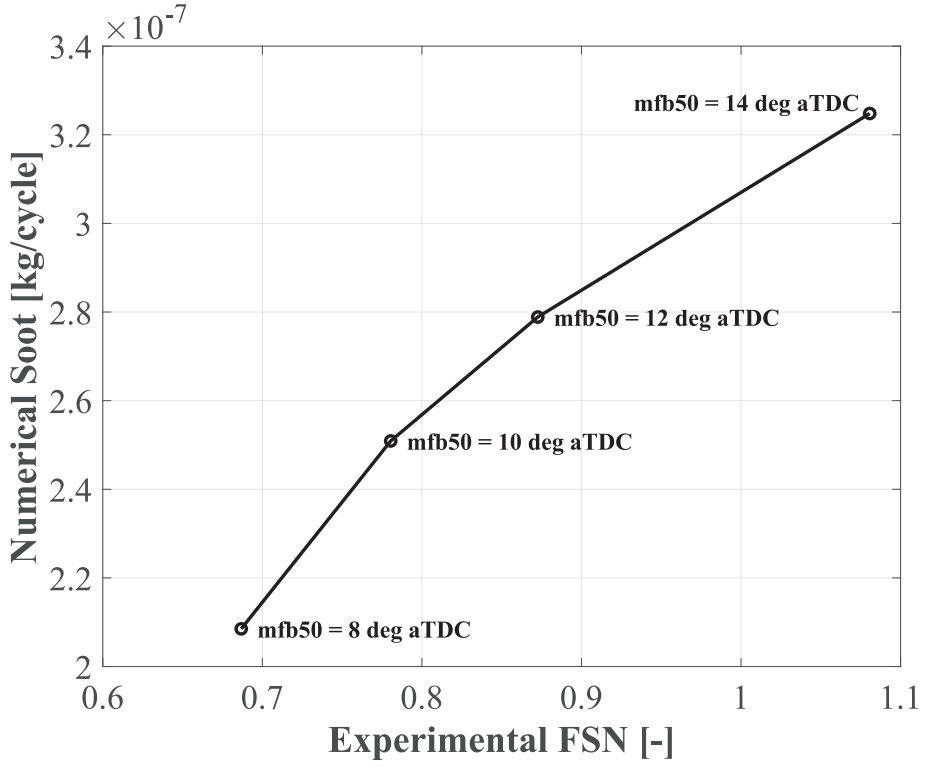

Fig. 7. Comparison between experimental FSN and corresponding simulated Soot concentration.

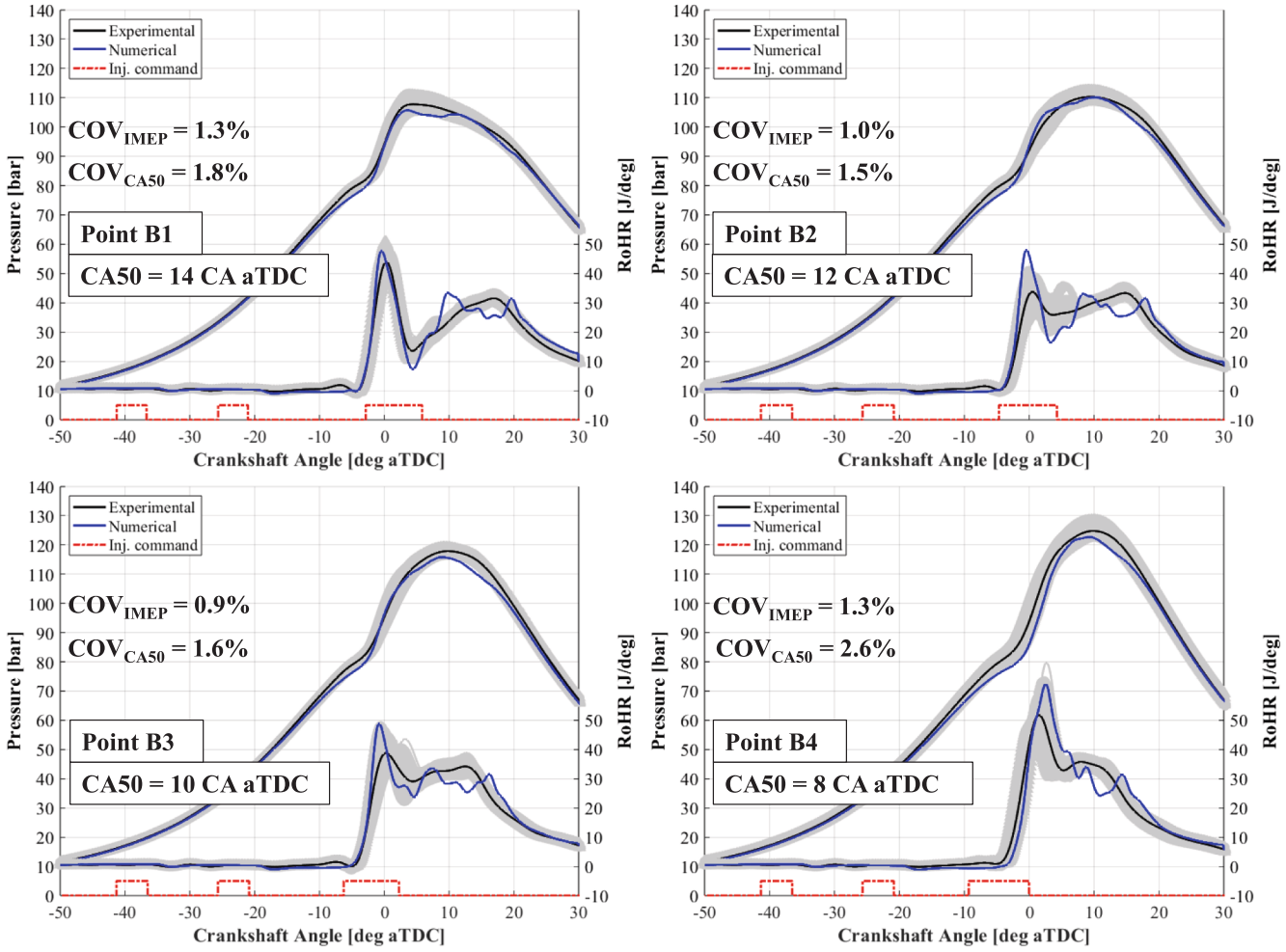

Fig. 8. Comparison between the experimental and simulated pressure and RoHR traces for Points B1 to Point B4.

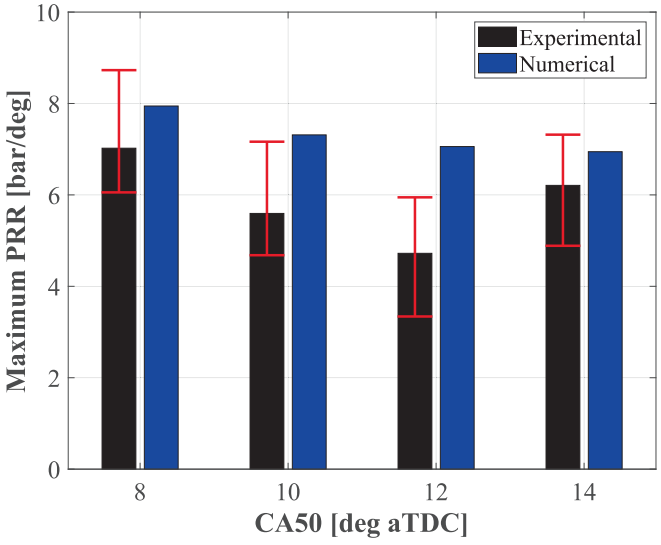

Fig. 9. Comparison between the experimental and simulated maximum PRR for Point B1 to B4.

to the maximum of the mean trace (black bars). Nevertheless, for these points, the predicted maximum PRR is close to the upper error bars, thus, they are in line with the maximum PRR of the faster cycle. It is visible that at higher load the PRR approaches the 10 bar/deg safety threshold, thus, at high load operations, the CFD prediction of the PRR would be overly cautions. Figs. 4, 5, 8, 9 reveal systematic under-prediction of pressure and overprediction of PRR likely due to the mis-capture of the Low-Temperature Heat Release. In experimental RoHR traces, the LTHR is visible slight before the premixed peak, while the PVM-MF model starts the combustion directly with the premixed phase. Therefore, the chemical energy of fuel is not staged in the very early ignition phase, leading to a steeper RoHR with a higher peak, resulting in the larger PRR.

The emissions analysis for the points B1-B4 is presented in Fig. 10 and Fig. 11. Fig. 10 shows that even at higher load and speed, the simulation is able to reproduce the effect of the CA50 on the ISNOX, the validation for the shorter CA50 is almost perfect but the model suffers from an accuracy loss for longer CA50 (12 deg aTDC and 14 deg aTDC). In Fig. 11 it is visible that at higher speed and load, the correlation between the experimental FSN and the simulated soot is weaker compared to that seen for points A1-A4. In fact, the data show a Pearson coefficient of 0.9 and a piece-wised shape mainly due to the loss of correlation strength for the longer CA50.

In light of the validation presented on pressure, RoHR, PRR, NOx and soot, the proposed CFD methodology can be considered reliable at medium–high load for comparative analysis between different injection

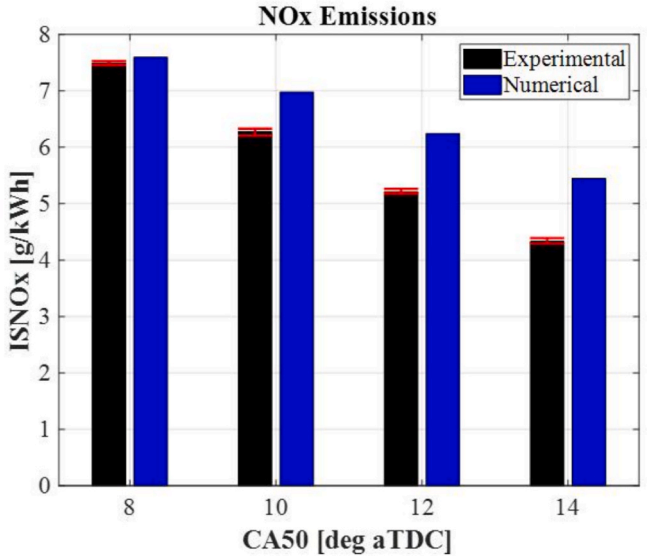

Fig. 10. Comparison between experimental and simulated ISNOx emissions for Points B1 to B4.

configurations. It is worth to mention that a perfect validation of the combustion and emission characteristics of low temperature combustion systems is hard to achieve. This is mainly due to the fact that the representation of LTCs strongly relies on several sub-models like the choice of a proper surrogate to describe the fuel evaporation rate and the mixing process, as well as a proper surrogate to describe the combustion and the corresponding kinetic scheme, as required by the model PVM-MF. Furthermore, it is remembered that LTCs are naturally more prone to cycle variations due to key importance of the local mixture distribution, which is characterized by natural randomness. Therefore, the experimental average cycle should not be seen as the reference to be strictly replicated.

The next section shows the investigation of the role of SOI timing in the GCI combustion by means of CFD simulations and the analysis of both mean results and three-dimensional fields in order to determines the modifications to implement on the injection pattern to improve the operations.

4. Results: Optimization of SOI-pilot and SOI-pre

In this section, the phasing of the Pilot and of the Pre injection events is discussed. The effect of the pressure wave propagation of the first pulse on the second one is neglected for simplicity. Hence, independently from the SOI of each pulse, the mass injected during each premixed injection event is the same. In order to optimize the injection patter via CFD simulations, the Point A3 of Table 5 has been considered as a baseline because of the better accuracy of the simulation shown in the validation step. Table 6 lists the different actuations tested for the SOI-Pilot and SOI-Pre.

From Test 1 to Test 4, only one pulse (the Pilot or the Pre) has been moved backward or upward with respect to the baseline configuration. From Test 5 to Test 8, both the pulses (Pilot and Pre) have been shifted. During all the tests, the SOI of the Main injection has been set at 2 deg bTDC, while the duration has been adjusted in order to ensure the introduction of a target fuel mass inside the cylinder (the same injected in the point A3). This choice is because the fair comparison between the tests, requires that the fuel mass introduced with the Pilot and the Pre is the same during the shift of the SOI.

Firstly, brief evaluation of the mutual influence between the SOI setting and the turbulence inside the cylinder is given (Fig. 12). Fig. 12 shows the value of the in-cylinder normalized Turbulent Kinetic Energy (u') against the SOI timing of Pilot (lower x-axis) and Pre (upper x-axis). Before Pilot, no injection events have occurred, thus, the only source of turbulence is the dissipation of the swirl motion into turbulence. Since at the tested SOI Pilot timings the swirl motion is still intense (swirl ratio around 2.8), u' is poor. The Pilot injection event promotes turbulence inside the chamber, in fact, the u' at any tested SOI Pre timing is higher.

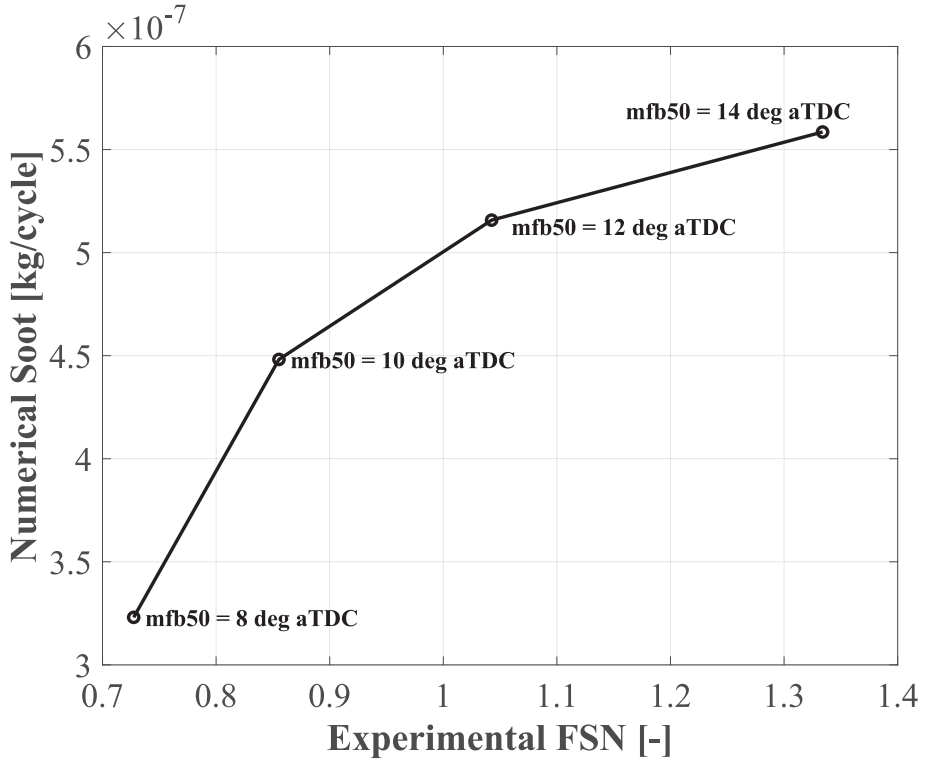

Fig. 11. Comparison between experimental FSN and corresponding simulated soot concentration for Points B1 to B4.

Table 6
Different SOI actuations for the Pilot and the Pre injections.

Test n°	SOI-Pilot [deg bTDC]	SOI-Pre [deg bTDC]	Dwell-time [CA deg]
Baseline (no wave)	35	21	10
Test 1	35	27	4
Test 2	35	15	16
Test 3	29	21	4
Test 4	41	21	16
Test 5	32	27	1
Test 6	29	15	10
Test 7	41	15	22
Test 8	41	27	10

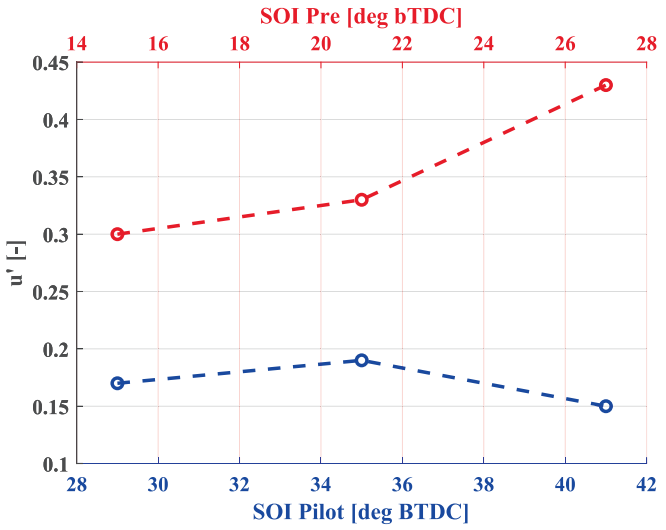

Fig. 12. Normalized turbulent kinetic energy depending on the timing of SOI Pilot (lower x) and SOI Pre (upper x).

Anticipating the SOI Pre (left to right on the upper x-axis) makes possible to start the second injection event in a more turbulent environment. However, because of the early time, in spite of the significant relative increase in u', the absolute value is not noteworthy. Therefore, it is not expected to find a key dependence between the dwell-time, the turbulence, and the combustion performance indicators.

Fig. 13 shows the effect of applying a different SOI-Pre while keeping fixed the SOI-Pilot. Considering to the blue curves, anticipating the Pre injection event leads to a slightly reduced peak of the premixed RoHR phase due to the resulting mixing. As a result, the peak RoHR in the premixed phase is comparable to the baseline, but the energy is released slowly, since the premixed stage is shifted slightly towards the expansion stroke. In this case, a slightly retarded SOC is attributed to the combination of: i) the cooling effect provided by the fuel evaporation; ii) the incomplete vaporization of the fuel introduced during the second pulse.

The first cause can be analysed in the equivalence ratio-temperature diagram shown in Fig. 14. Each point in the diagram is obtained by associating the values of temperature and equivalence ratio in each cell of the CFD domain at a given time-step. Therefore, each coloured scatter gives information on the local fuel and temperature distribution inside the piston bowl at 720 CA deg for a specific injection pattern. The final aim of this diagram is to determine the effect of the SOI-Pre and SOI-Pilot shift on the mixture-temperature conditions at the beginning of the combustion trigger, namely the main injection event.

In Fig. 14 it is visible that the fuel-temperature distributions inside the piston bowl for Test 1 and Test 2 have the same shape as that of the Baseline. Focusing on the high-temperature region (temperature above 1200 K) Test 1 shows a leaner distribution because of the anticipated SOI-Pre (higher mixing time), in fact, the blue scatter is denser at lower values compared to the black one. On the other hand, the retarded condition (Test 2) leads to slightly richer regions, in fact, the red scatter has a higher maximum value of the equivalence ratio as well as a denser distribution in the upper region. This finding matches with the values of skewness and kurtosis of both temperature and equivalence ratio (Fig. 14, right). In fact, anticipating the Pre injection leads to a reduction in the skewness and kurtosis for both variables, indicating a more symmetrical and less-tailed distribution.

Concerning the second cause of the delayed SOC, the cooldown

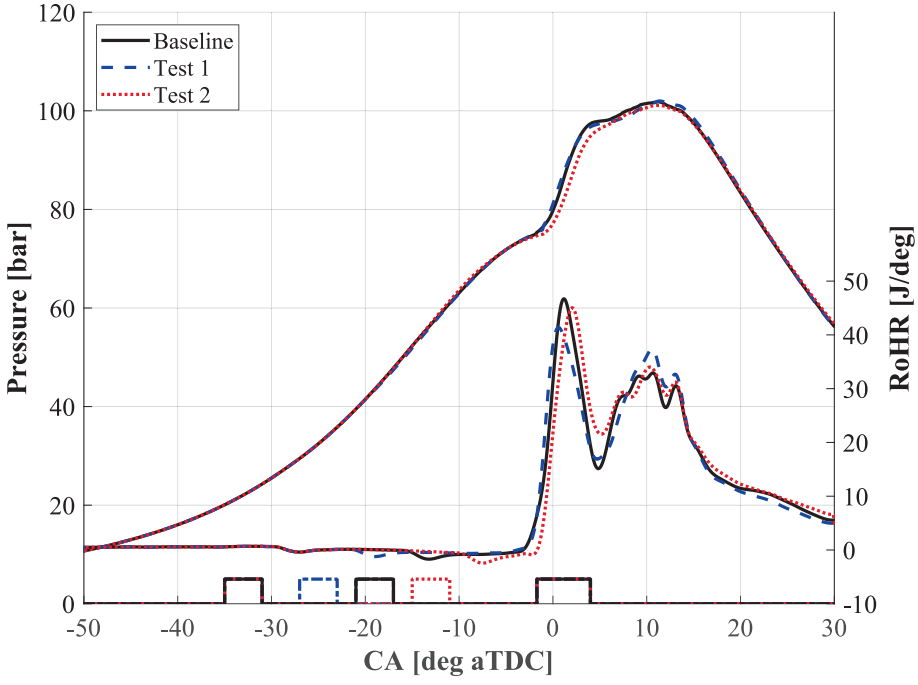

Fig. 13. Pressure and RoHR traces with fixed SOI-Pilot and different SOI-Pre (Baseline, Tests 1 and 2).

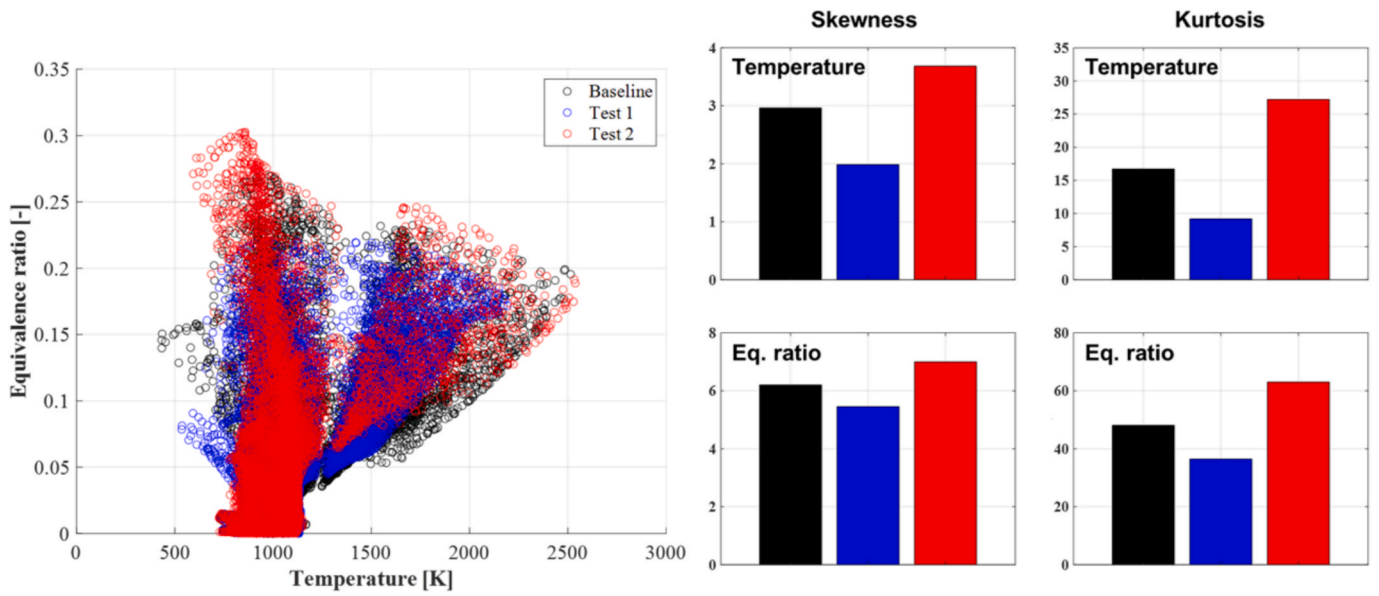

Fig. 14. Comparison of the local temperature and equivalence ratio between Baseline, Test 1 and Test 2 at the firing TDC. Skewness and kurtosis of the distributions are also reported.

promoted by the delayed SOI-Pre is proven by the distribution of the red scatter along the temperature axis. In fact, the red scatter is significantly sparser than the blue and the black ones in the high temperature (> 1200 K) region. Furthermore, as visible in Fig. 15, the retarded SOI configuration (Test 2) is characterized by a larger number of droplets (fuel in the liquid phase) inside the bowl compared to the other two configurations. Overall, the importance of the SOI-Pre is limited since it does not produce significant modifications to the shape of the RoHR and to the SOC of the diffusive phase.

In order to provide insights on the role of the SOI of the first two pulses, a statistical analysis has been performed on the three-dimensional field of the fuel concentration inside the domain (Fig. 16). In particular, the cells where a concentration of the fuel vapor phase larger than 1 % have been selected. Then, the data inside each cell comprised in the subset have been processed to determine the instantaneous values for: i) median; ii) standard deviation; iii) volume occupied by these cells over the available instantaneous cylinder volume (in percentage). Fig. 16 shows the abovementioned quantities for Tests 1 and 2 comparing the results with the Baseline condition.

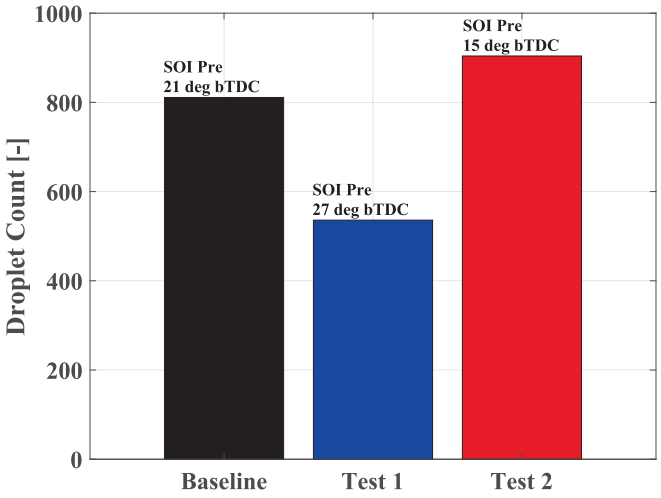

Fig. 15. Comparison of the liquid droplet count between Baseline, Test 1 and Test 2 at the firing TDC.

Regarding Test 1, the SOI-Pre is anticipated compared to the Baseline pattern. This condition enhances the fuel vaporization due to the longer time available for the phase change. Consequently, the mixture is less stratified, in fact, the standard deviation at the SOI-Main time is reduced (Fig. 16b), and a larger volume is occupied by a significant amount of vapor fuel (Fig. 16c). However, at the SOI-Main time, the values of the distributions appear very similar compared to the Baseline configuration, confirming the marginal effect that the SOI-Pre.

The shifting of the Pilot injection is more effective on the shape of the RoHR (Fig. 17). The more the SOI-Pilot is anticipated, the longer is the time available for a proper mixing with the air. As a result, the distribution of fuel inside the combustion chamber features smaller gradients. Furthermore, the cooling effect provided by the fuel evaporation will be shared with a larger amount of air. This can be seen comparing the scatters in Fig. 14 and Fig. 18, in fact, the red and blue scatters are denser in the low temperature region (< 1200 K) with a coarse presence of points out of the main area.

Similarly to tests 1 and 2, anticipating the Pilot injection results in increased symmetry and less-tailed distribution, as skewness and kurtosis of the data highlight in Fig. 18. The RoHR generated with a more anticipated SOI-Pilot (Test 4) reaches lower peaks during the premixed phase. The stratified mass that did not burn during the premixed phase, releases the energy during the diffusive stage together with the fuel mass injected in the Main pulse. This can be seen by focusing on the trends of the blue RoHR during the diffusive stage. It is interesting to notice that the peak value of the blue RoHR is almost the same for both the combustion stages (premixed and diffusive) showing a smoother burn rate. Retarding the SOI-Pilot (Test 3, red curves) leads to a larger presence of fuel inside the piston bowl region (Fig. 18, the red scatter spreads higher equivalence ratio values), thus, to a higher energy released during the premixed phase.

Focusing on Fig. 19a the shape of the median values produced by the different Pilot pulses are almost the same, but they shift according to the pattern. For the most anticipated Pilot injection, the median is the lowest, and the opposite trend is reported for the most retarded pulse. Consequently, as anticipated earlier, this result proves that, for the most anticipated case, the fuel has more time to properly mix with air. This is also confirmed by the lower standard deviation (Fig. 19b), which reveals a weaker stratification level in the combustion chamber. Concerning the volume fraction in Fig. 19c, before SOI-Pre, higher values are reported for Test 4, as expected. Then, after the Pre injection, the volume fraction

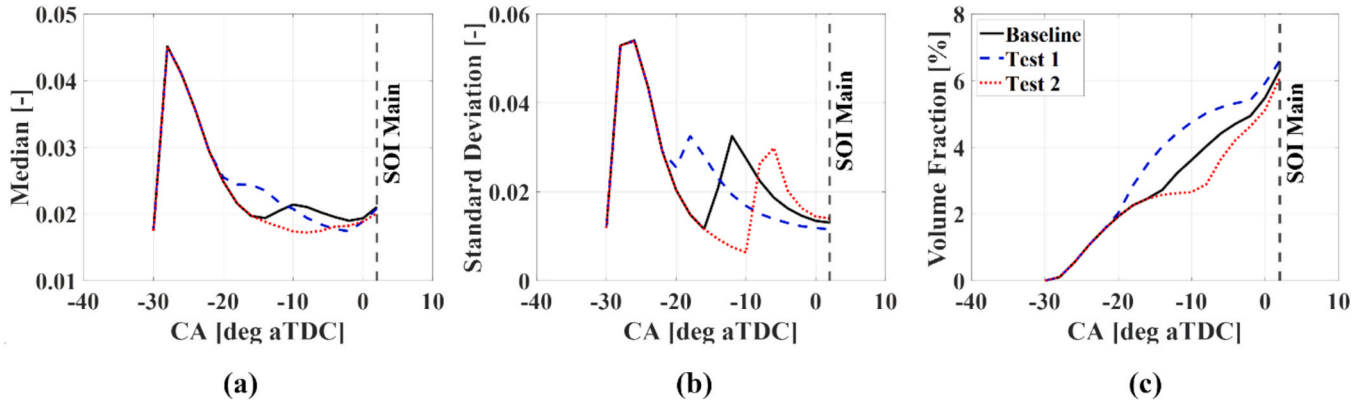

Fig. 16. Comparison between the Baseline, Test 1 and Test 2 on the Median (a), Standard Deviation (b), and Volume Fraction (c) of the fuel injected by Pilot and Pre pulses.

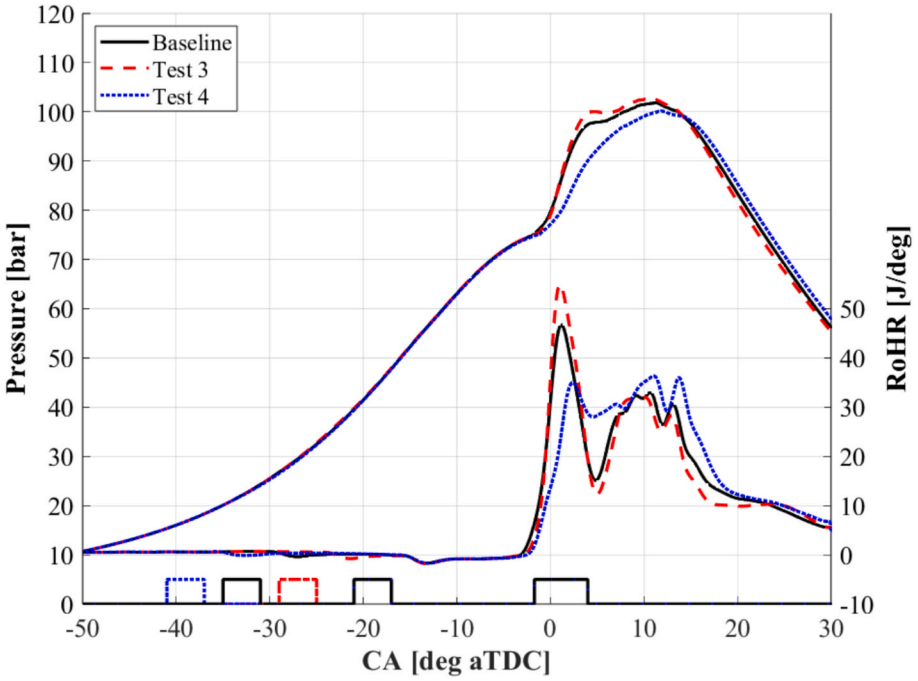

Fig. 17. Pressure and RoHR traces with fixed SOI-Pre and different SOI-Pilot (Baseline, Test 3 and Test 4).

trends are almost the same.

The effect of the simultaneous variation of both SOI-Pilot and Pre injections is shown in Fig. 20. Starting from the traces of Test 5, an earlier premixed heat release can be seen due to the relatively close position of the pulses (Test 5 has the shortest dwell-time). The total fuel injected before the main injection generates a highly stratified charge which leads the SOC to be anticipated. This effect is similar to that seen in Test 1, for which the Pre injection moved towards the Pilot one. On the other hand, the RoHR relative to the Test 6 exhibits the highest peak. As seen in Test 3, retarding the Pilot injection leads the premixed phase to release more energy. The last two test cases (Test 7 and 8) are generated imposing the most anticipated SOI-Pilot and two different SOI-Pre.

In Test 7, the first two pulses are actuated with the longest dwell-time (22 CA), while in Test 8, the two pulses are actuated with the same dwell-time as that of the baseline (10 CA) but both the pulses are anticipated. Compared to Test 4, which had the same SOI-Pilot, the premixed and diffusive stages appear more separate due to the more retarded SOI-Pre. Anticipating the SOI-Pilot helps increasing the RoHR during the diffusive stage. This trend is consistent with the one shown during Test 4. Moreover, the more retarded the SOI-Pre is, the higher will be the RoHR trace during the diffusive combustion (Tests 7 and 8). This is due to the different timing at which the fuel is available to auto ignite. It is worth to mention the behaviour of median and standard deviation of Test 7 in Fig. 21a and Fig. 21b, respectively. In fact, Test 7 combines the effects of both a retarded SOI-Pre (Test 2) and anticipated SOI-Pilot (Test 4). The most retarded Pre injection leads to generate a stronger stratification level, as Fig. 19b highlights. Moreover, the most anticipated Pilot pulse allows an overall leaner mixture.

To further analyse the effect of the injection pattern on the combustion development, the crank angle at which the 10 %, 50 % and 90 % Mass Fuel Burnt (MFB10, MFB50 and MFB90, respectively) occurs can be insightful. As visible in Fig. 22, the effect of different SOI timings is more pronounced during the early combustion phase (MFB10). In fact, Fig. 22a, reports a strong variation of the CA10 associated to the tests listed in Table 6. A shorter dwell-time between the injection events (Tests 1, 3, 5) leads to a shorter SOC due to the higher level of stratification. Test 5 exhibits the shortest CA10 because, in this case, the dwell-time between Pilot and Pre pulses is the shortest (1 CA) resulting in enhanced stratification, with richer pockets of mixture that can easily

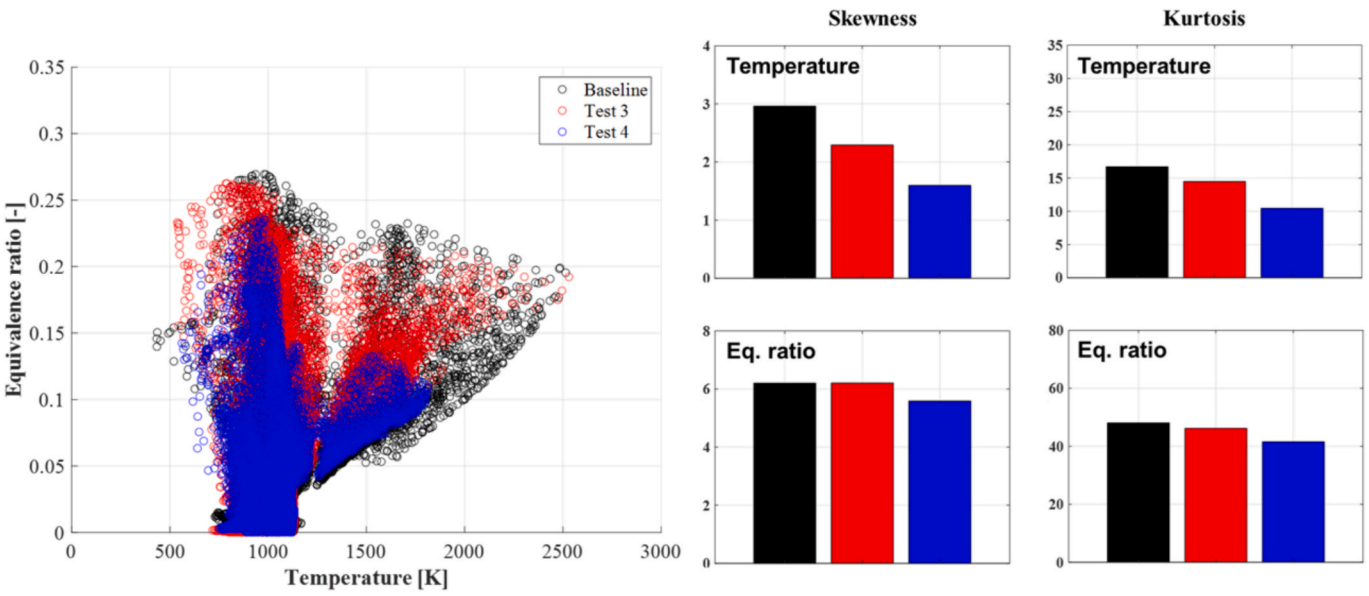

Fig. 18. Comparison of local temperature and equivalence ratio between the Baseline, Test 3 and Test 4 at the firing TDC. Skewness and kurtosis of the distributions are also reported.

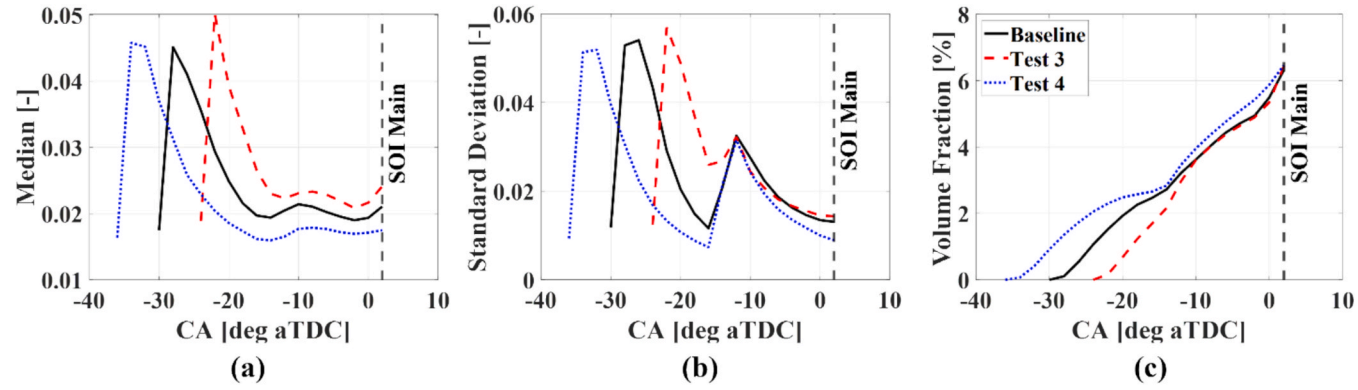

Fig. 19. Comparison between the Baseline, Test 3 and Test 4 on the Median (a), Standard Deviation (b), and Volume Fraction (c) of the fuel injected by Pilot and Pre pulses.

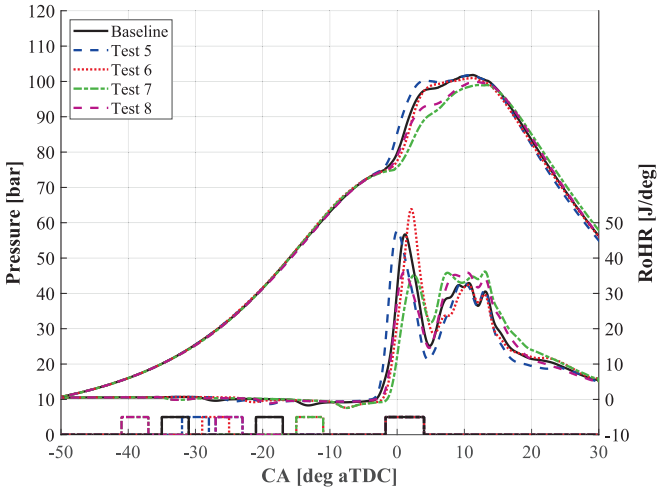

Fig. 20. Pressure and RoHR traces with varying both SOI-Pilot and Pre (Tests Baseline, 5, 6, 7, and 8).

auto-ignite. Instead, implementing a larger distance between the pulses (Tests 2, 4,7) promotes a delayed SOC compared to Baseline and Tests 6, 8. Concerning the CA50, Fig. 22b highlights that the variation with respect to the Baseline condition is less pronounced, since the Main injection, which provides most of the fuel mass, is fixed. However, small variations of the CA50 are responsible for significant variations of the indicated efficiency (from + 3 % to −4% compared to the baseline), as will be shown below. The value of the CA90 in Fig. 22c is almost insensitive to a different SOI for Pilot and Pre injections. This is reasonable since, from CA50 on, the combustion proceeds by diffusion consuming the fuel mass introduced with the Main injection.

Fig. 23 highlights the different PRR obtained varying the SOI-Pre and Main. The highest PRR values occur for the most retarded conditions for the SOI-Pilot. In fact, for those conditions, the richer regions generated by the retarded injections produce a high energy release in a short time. Instead, having more homogeneous regions is effective for the PRR mitigation due to higher reactivity stratification [30,31]. Consequently, the reduction in NOx emission for more reactivity-stratified conditions is due to the reduced temperatures inside the combustion chamber [32].

The response of the engine in terms of performance and emissions to the injection pattern has been then mapped in Fig. 24, in which the values of indicated efficiency, soot, NOx, and CO are shown in percentage variation compared to the Baseline configuration. Regarding the

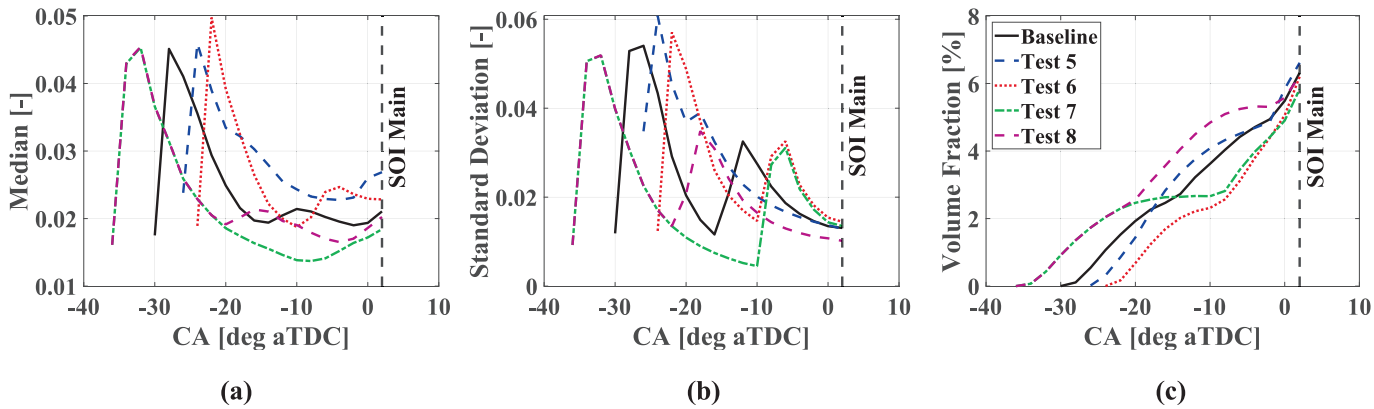

Fig. 21. Comparison between the Baseline, Test 5 to Test 8 on the Median (a), Standard Deviation (b), and Volume Fraction (c) of the fuel injected by Pilot and Pre pulses.

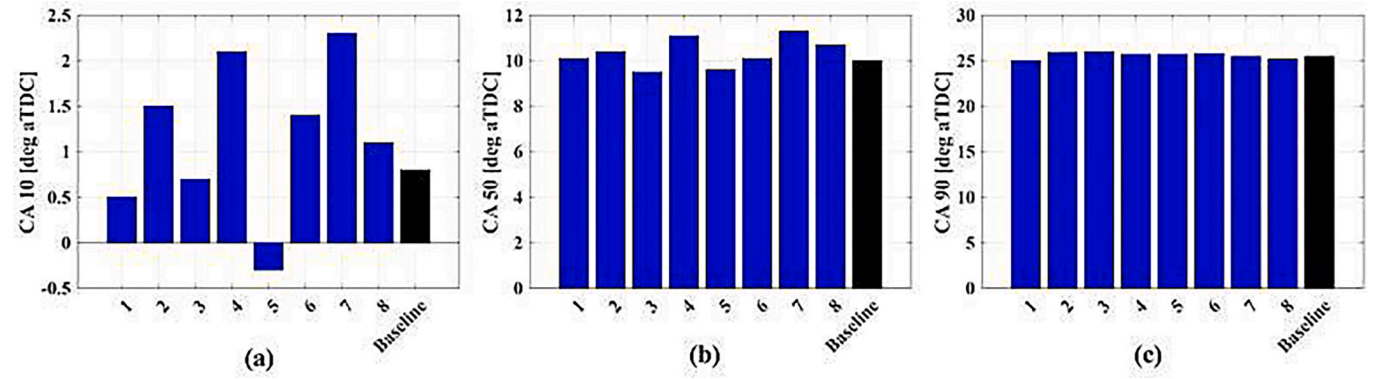

Fig. 22. Comparison between the Baseline and the Tests for CA10, CA50 and CA90.

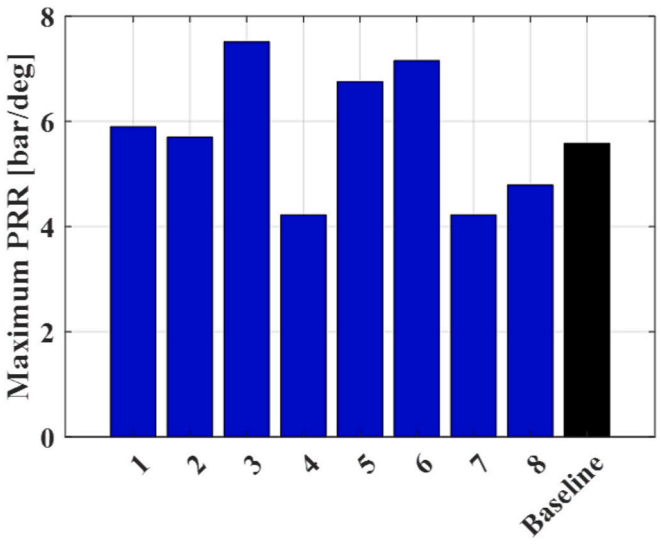

Fig. 23. Comparison between Baseline and the Tests for PRR.

trend of the indicated efficiency in Fig. 24a, the map demonstrates that setting a larger distance between the Pre and Pilot injections is effective to increase the engine efficiency. In fact, the highest indicated efficiency is reached in Test 7, namely the one with the longer dwell-time. In this condition, the CA50 is delayed compared to the Baseline condition, owing to a better chemical-to-mechanical conversion. The increased indicated efficiency improves the fuel economy, in fact, as the same fuel mass injected provides a higher indicated work if the pattern of Test 7 is used, the mass introduced during the Main injection can be decreased resulting in lower CO_2 produced to fulfil the target IMEP. Anticipating the SOI-Pre leads to an increase in soot emissions (Fig. 24b). This trend comes from the different distribution of fuel inside the combustion chamber. In fact, anticipating the SOI-Pre generates richer regions which are less likely to be oxidised. Soot emissions can be smoothed by anticipating the SOI-Pilot as well. In fact, Test 7 provides a consistent reduction in soot emission.

The improved chemical-to-mechanical efficiency promoted by a longer dwell-time results in a reduced temperature inside the cylinder, thus, lower NOx emissions are found (Fig. 24c). The map shows that the NOx reduction is mainly provided by the shift backward of the SOI-Pilot. In fact, the more anticipated is the Pilot injection, the less stratified is the mixture. Consequently, each cell of the domain is characterized by a leaner composition falling inside the flammability limits. This condition reduces the NOx formation due to the lower temperatures involved. The cause of reduction in NOx emissions can be seen in Fig. 25, which shows the temperature and equivalence ratio scatter for the Baseline and the Test 7. Each point shown in Fig. 25 represents the pair of values in a single cell inside the cylinder before the Main pulse. Consequently, they reflect only the contributions of different injection strategies during the premixed pulses. For Test 7, the fewer number of points lying on the high-temperature region of the diagram allows the generation of a reduced quantity of NOx compared to the Baseline configuration.

The CO emission (Fig. 24d) is dependent on the relative distance between the two injections. In fact, compared to the Baseline condition, no variation in CO emissions is reported with anticipated SOI-Pilot and retarded SOI-Pre (white arrow). On the other hand, making the injections closer leads to a slight increase in CO emissions. This increment

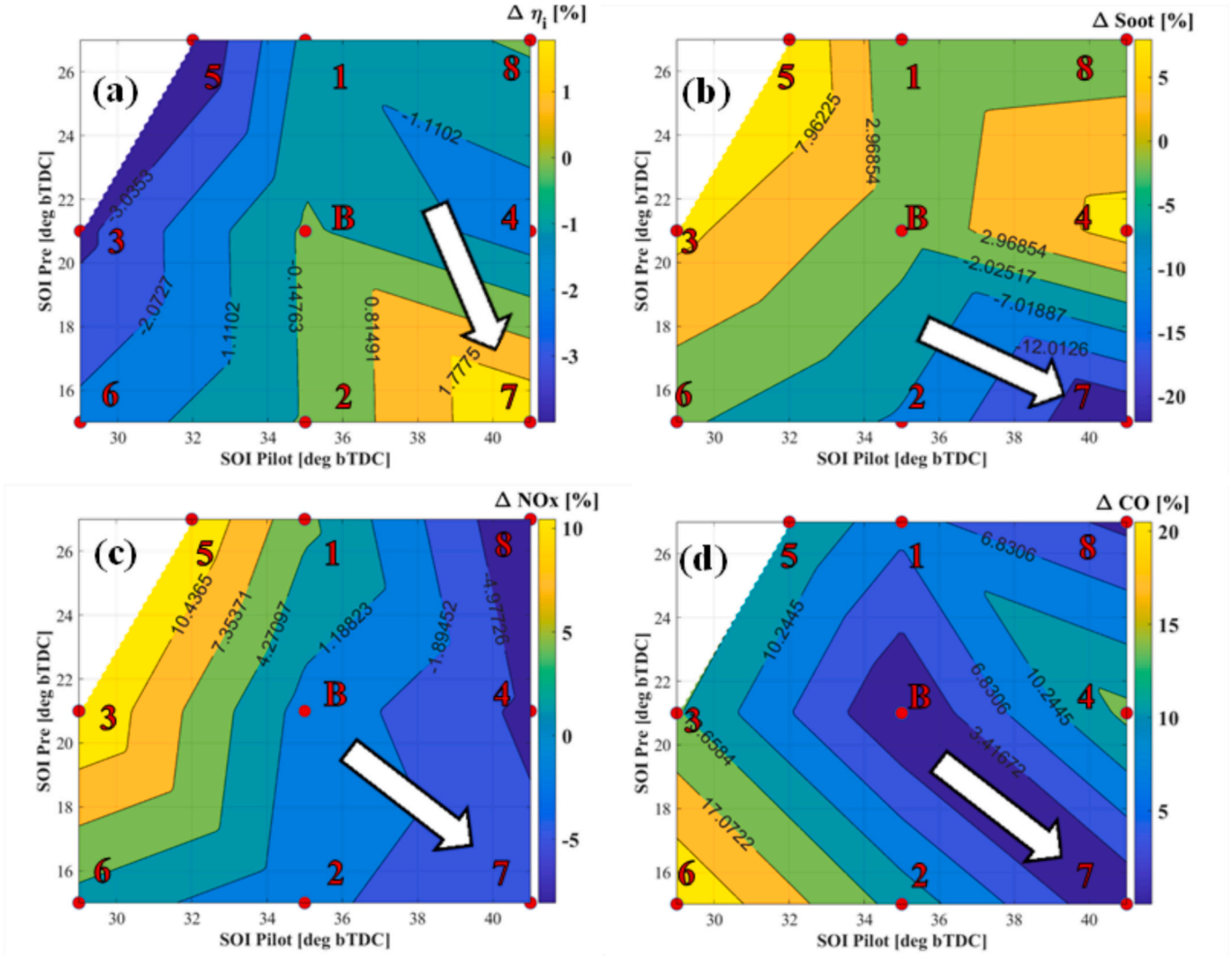

Fig. 24. Heatmap showing the variation of indicated efficiency (a), soot (b), NOx (c), and CO (d) according to the SOI-Pilot and SOI-Pre.

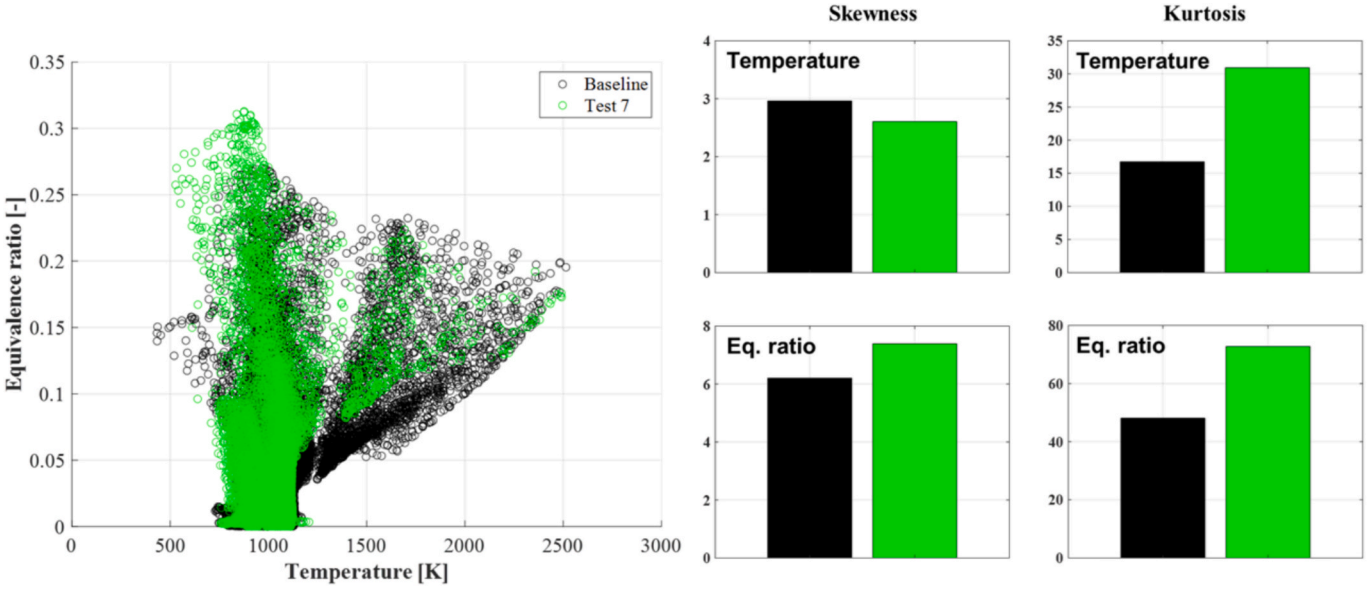

Fig. 25. Local temperature-equivalence ratio diagram inside the combustion chamber for Baseline and Test 7 at the firing TDC. Skewness and kurtosis of the distributions are also reported.

is more pronounced if the SOI-Pre is moved, since an increment of more than 20 % is reported. This is due to the local richer conditions inside the combustion chamber promoted by the reduced dwell-time. In fact, as in Fig. 21a, the median of fuel injected for Tests 5 and 6 are the highest. This is due to a reduced mixing capability provided by the closer injection pattern.

Fig. 26 reports a summary of the variation of CO, NOx, soot, indicated efficiency and PRR with respect to the baseline condition considering the optimized injection pattern (Test 7). Fig. 26 provides insightful guidelines about the role of Pilot and Pre injections to significantly improve different key engine aspects. The longest dwell-time combined with a specific anticipation of the SOI-Pilot leads to: i) almost the same CO emission (+0.3 %); a strong reduction of soot emissions (–22 %); iii) a slight reduction of NOx emission (−3.7 %); iv) a significant gain in the indicated efficiency (+2.7 %); v) a strong reduction of the PRR (−25 %), which allows to operate the considered point in a safer manner. These values are promising for the simultaneous reduction of the pollutants produced by the studied engine, and they open the room to improve the GCI setup. Focusing on different injection patterns, Fig. 24 highlights an overall detrimental effect when injection events are closer between each other and when the TDC is approached. In fact, especially for tests 3, 5, 6, an overall reduction in efficiency is followed by increased pollutant emissions. As highlighted previously, the insufficient time for mixing (which is shown also in Figs. 16, 19 and 21) makes the overall combustion process less efficient.

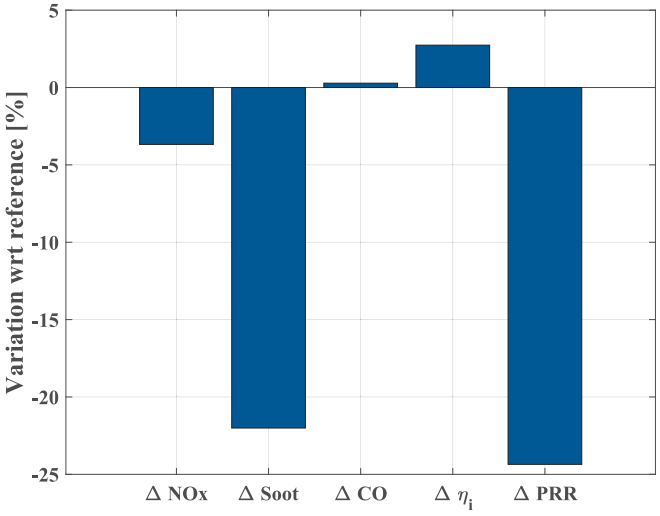

Fig. 26. Gains and losses of Test 7 compared to the baseline in terms of NOx, soot, CO, indicated efficiency and PRR.

5. Conclusion

This paper deals with the CFD analysis and optimization of the injection pattern to operate a PPCI combustion at engine mid-high load. The simulations have been conducted on the CAD model of a real light-duty engine which features a flat head and a piston bowl. The CFD methodology has been setup to capture the combustion phases (premixed and diffusive) typical of PPCI without using a detailed chemical kinetics solver and automatic mesh refinement, to achieve reliable results with affordable expense of computing power and time.

The ability of the CFD model to reproduce the behaviour of the real PPCI engine has been tested considering three closely spaced injection events, which has been poorly investigated in the literature compared to single injection PPCI operations. The first two pulses (Pilot and Pre) are beneficial to accelerate the auto ignition of the last one (Main). The validation matrix includes two different mid-high loads and four different CA50. Different injection patterns obtained by shifting the SOI of the Pilot and the Pre have been explored to design a new injection pattern that yields an improved trade-off in terms of emissions, efficiency and durability. The main outcomes of the investigation are resumed:

- The progress variable combustion model supported by a proper setting of the spray models can match (in some cases even outperform) detailed chemical kinetics solver-based simulations in reproducing the shape (pressure trace and RoHR) and emissions of PPCI with limited computing power and simulation time.
- The simulated maximum PRR values, pressure traces and the RoHR profiles are in line with the experimental ones, lying in the range of the real cycle to cycle variability of the engine. At IMEP = 10 bar, the indicated specific NOx emissions are reproduced with nice accuracy (max relative error around 6 %) at any CA50, whilst at IMEP = 14 bar, the accuracy falls for the points with longer CA50.
- After the test of 8 new design of the injection pattern, a complex dependence of NOx, soot, CO, efficiency on the shift of the SOI (both Pilot and Pre) and of the dwell time has risen. From the standpoint of NOx and efficiency, the influence of shifting the SOI-Pre is weak, whilst advancing the SOI-Pilot is crucial to reduce NOx emissions while increasing the efficiency. However, for the most advanced SOI-Pilot, slightly delaying the SOI-Pre helps to further increase the efficiency. Soot and CO are highly sensitive to the shift of both SOI-Pilot and SOI-Pre as well as to the dwell time between the two with a non-monotonous behaviour. Even for CO and soot, a higher anticipation of the SOI-Pilot yields better results if coupled with the delay of the SOI-Pre.
- According to the mapped effect of the SOI shift, a new pattern characterized by SOI-Pilot of 41 CA degBTDC (6 CA deg anticipated compared to the baseline), a SOI-Pre of 15 CA degBTDC (6 CA deg delayed compared to the baseline), and SOI-Main of 1.7 CA degBTDC. This design allows a decent increase of efficiency (roughly + 3 %), a significant reduction of NOx emissions (roughly −5%), and a strong reduction of soot (–22 %) and maximum PRR (−25 %). It is underlined that this guideline for the injection pattern design is suitable for points similar to the tested ones (mid-high load), while its validity on off-design operations (cold states, low load, high EGR) is not demonstrated.

CRediT authorship contribution statement

Davide Viscione: Writing – original draft, Software, Methodology, Investigation, Conceptualization. **Valerio Mariani:** Writing – review & editing, Writing – original draft, Methodology, Investigation, Conceptualization. **Gian Marco Bianchi:** Writing – review & editing, Supervision, Software. **Stefania Falfari:** Writing – review & editing, Supervision, Resources. **Vittorio Ravaglioli:** Validation, Supervision, Resources, Conceptualization. **Giacomo Silvagni:** Writing – review & editing, Validation, Conceptualization.

Declaration of competing interest

The authors declare that they have no known competing financial interests or personal relationships that could have appeared to influence the work reported in this paper.

Data availability

Data will be made available on request.

References

[1] Emission Standards: Europe: Cars and Light Trucks, https://dieselnet.com/standards/eu/ld.php#stds (accessed July 17, 2024).
[2] C. Moll, A. Durand, C. Rohde, Preparatory study on ecodesign and energy labelling of batteries – TASK 3 report users, 2019 (accessed July 17, 2024).

[3] F. Alanazi, Electric vehicles: benefits, challenges, and potential solutions for widespread adaptation, Appl. Sci. 13 (10) (2023), https://doi.org/10.3390/app13106016.
[4] M. Sellnau, J. Sinnamon, et al., Gasoline direct compression ignition (GDCI)-diesel-like efficiency with low CO_2 emissions, SAE Int. J. Engines 4 (1) (2011), https://doi.org/10.4271/2011-01-1386.
[5] S. Chu, J. Lee, et al., High load expansion with low emissions and pressure rise rate by dual-fuel combustion, Appl. Therm. Eng. 144 (2018), https://doi.org/10.1016/j.applthermaleng.2018.08.027.
[6] J. Kang, S. Chu, et al., Effect of operating parameters on diesel/propane dual fuel premixed compression ignition in a diesel engine, Int. J. Automot. Tech. 19 (2018), https://doi.org/10.1007/s12239-018-003-6.
[7] J. Paz, D. Staaden, S. Kokjohn, Gasoline compression ignition operation of a heavy-duty engine at high load, SAE Tech. (2018), https://doi.org/10.4271/2018-01-0898, 2018–01-0898.
[8] M. Sellnau, M. Foster, et al., Pathway to 50% brake thermal efficiency using gasoline direct injection compression ignition, SAE Int. J. Adv. Curr. Prac. Mobility 1 (4) (2019), https://doi.org/10.4271/2019-01-1154.
[9] M. Sellnau, J. Sinnamon, et al., Full-time gasoline direct-injection compression ignition (GDCI) for high efficiency and low nox and PM, SAE Int. J. Engines 5 (2) (2012), https://doi.org/10.4271/2012-01-0384.
[10] A.K. Agarwal, V.S. Solanki, M. Krishnamoorthi, Experimental evaluation of pilot and main injection strategies on gasoline compression ignition engine-part 1: combustion characteristics, SAE Int. J. Engines 16 (6) (2023), https://doi.org/10.4271/03-16-06-0046.
[11] S. Curran, J. Szybist, B. Kaul, et al., Fuel stratification effects on gasoline compression ignition with a regular-grade gasoline on a single-cylinder medium-duty diesel engine at low load, SAE Int. J. Adv. Curr. Prac. Mobility 4 (2) (2021), https://doi.org/10.4271/2021-01-1173.
[12] J. Badra, A. Zubail, J. Sim, Numerical investigation into effects of fuel physical properties on GCI engine performance and emissions, Energy Fuels 33 (2019), https://doi.org/10.1021/acs.energyfuels.9b02340.
[13] J. Badra, F. Khaled, et al., Combustion System optimization of a light-duty GCI engine using CFD and machine learning, SAE Tech. (2020), https://doi.org/10.4271/2020-01-1313, 2020–01-1313.
[14] J. Sim, J. Chang, J. Badra, Co-optimization of piston bowl and injector for light-duty GCI engine using CFD and ML, Fuel 329 (2022), https://doi.org/10.1016/j.fuel.2022.125455.
[15] S. Kim, J. Kim, Numerical study of advanced compression ignition and combustion in a gasoline direct injection engine, ASME 2019 Int. Combust. Engines Div. Fall Tech. Conf. (2019), https://doi.org/10.1115/ICEF2019-7281.
[16] S.K. Addepalli, M. Pamminger, et al., Modeling the impact of the fuel injection strategy on the combustion and performance characteristics of a heavy-duty GCI engine, Int. J. Engine Res. 25 (1) (2024), https://doi.org/10.1177/14680874231206650.
[17] A.A. Moiz, K. Cung, Investigation of gasoline compression ignition in a heavy-duty diesel engine using computational fluid dynamics, SAE Tech. (2021), https://doi.org/10.4271/2021-01-0493, 2021–01-0493.
[18] J. Sim, J. Chang, J. Badra, CFD-guided optimization of the injector and injection parameters for light-duty GCI engine, Fuel 316 (2022), https://doi.org/10.1016/j.fuel.2022.123389.
[19] F. Stola, V. Ravaglioli, et al., Injection Pattern investigation for gasoline partially premixed combustion analysis, SAE Tech. (2019), https://doi.org/10.4271/2019-24-0112, 2019–24-0112.
[20] D. Viscione, G.M. Bianchi, et al., 1D-3D coupled approach for the evaluation of the in-cylinder conditions for gasoline compression ignition combustion, J. Phys. Conf. Ser. 2385 (2022), https://doi.org/10.1088/1742-6596/2385/1/012067.
[21] D. Viscione, V. Ravaglioli, et al., CFD methodology to capture the combustion behavior of a conventional diesel engine retrofitted to operate in gasoline compression ignition mode, Energies 17 (2024), https://doi.org/10.3390/en17164061.
[22] D. Viscione, V. Mariani, et al., Unconventional gasoline spray injection events: compared evolution of experimental data and numerical solutions, Fuel 355 (2023), https://doi.org/10.1016/j.fuel.2023.129438.
[23] D. Viscione, V. Mariani, et al., Investigation of the GCI main injection: experimental-numerical analysis of gasoline spray impact at reference engine conditions, Int. J. Multiphase Flow 182 (2025), https://doi.org/10.1016/j.ijmultiphaseflow/2024.105034.
[24] T. Bo, R. Rawat, et al., Multi-fuel and mixed-mode IC engine combustion simulation with a detailed chemistry based progress variable library approach, In: Int. Symp. Diagn. Model. Combust. Intern. Combust. Engines 8 (2012), https://doi.org/10.1299/jmsesdm.2012.8.146.
[25] D.L. Baulch, M. Bowers, et al., Homogeneous gas phase reactions of the hydroxyl radical with alkanes, J. Phys. Chem. Ref. Data 15 (1986) 101063/1555774.
[26] A. Karlsson, I. Magnusson, et al., Simulation of soot formation under diesel engine conditions using a detailed kinetic soot model, SAE Tech. (1998) 981022, https://doi.org/10.4271/981022.
[27] D.J. Hautman, F.L. Dryer, et al., A multiple-step overall kinetics mechanism for the oxidation of hydrocarbons, Combust. Sci. Tech. 25 (1981), https://doi.org/10.1080/00102208108547504.
[28] T.J. Pilusa, M.M. Mollagee, E. Muzenda, Reduction of vehicle exhaust emissions from diesel engines using the whale concept filter, Aerosol. Air Qual. Res. 12 (2012), https://doi.org/10.4209/aaqr.2012.04.0100.
[29] V. Prikhodko, S. Curran, et al., Emission characteristics of a diesel engine operating with in-cylinder gasoline and diesel fuel blending, SAE Int. J. Fuels Lubr. 3 (2) (2010), https://doi.org/10.4271/2010-01-2266.
[30] J. Li, X. Yu, et al., Mitigation of high pressure rise rate by varying IVC timing and EGR rate in an RCCI engine with high premixed fuel ratio, Energy 192 (2020), https://doi.org/10.1016/j.energy.2019.116659.
[31] J. Li, W.M. Yang, et al., Numerical investigation on the effect of reactivity gradient in an RCCI engine fueled with gasoline and diesel, Energy Convers. Manag. 92 (2015), https://doi.org/10.1016/j.enconman.2014.12.071.
[32] N. Horibe, T. Ishiyama, Relations among nox, pressure rise rate, HC and CO in LTC operation of a diesel engine, SAE Tech. (2009), https://doi.org/10.4271/2009-01-1443, 2009–01-1443.